Energy Conversion and Management: X 30 (2026) 101575

Contents lists available at ScienceDirect

Energy Conversion and Management: X

journal homepage: www.sciencedirect.com/journal/energy-conversion-and-management-x

Passively-tuned roll-based wave energy converter for enhanced efficiency and frequency adaptability

Ruben J. Paredes [a,b,*], David Plaza [b], Raju Datla [b], Mijail Arias-Hidalgo [c], Paul S. Zambrano [a], Jose R. Marin-Lopez [a], Jose M. Ahumada [d], Ricardo Álvarez-Briceño [e], Rafael Soria [f], Wilson Guachamin-Acero [e], Jesus Portilla-Yandun [e], Muhammad R. Hajj [b]

[a] ESPOL Polytechnic University, ESPOL, Faculty of Maritime Engineering and Marine Sciences, Km. 30.5 Vía Perimetral, Guayaquil, 090902, Guayas, Ecuador
[b] Stevens Institute of Technology, Davidson Laboratory, 711 Hudson St, Hoboken, 07030, NJ, USA
[c] ESPOL Polytechnic University, ESPOL, Faculty of Geosciences Engineering, Water Centre for Sustainable Development (CADS), Km. 30.5 Vía Perimetral, Guayaquil, 090902, Guayas, Ecuador
[d] Inst. of Naval Architecture and Ocean Engineering, Universidad Austral de Chile, Gral Lagos 2086, Valdivia, 170901, Los Rios, Chile
[e] National Polytechnic School - EPN, Department of Mechanical Engineering, Ladron de Guevara E11-253, Quito, 170525, Pichincha, Ecuador
[f] San Francisco University of Quito, Institute of Energy and Materials, Diego de Robles and Interoceanica St, Quito, 170901, Pichincha, Ecuador

ARTICLE INFO

Keywords:
Capture width ratio
Passive tuning
Roll motion
Submerged cones
WEC

ABSTRACT

Wave Energy Converters (WECs) typically exhibit natural oscillation frequencies that are significantly higher than the dominant frequencies of ocean waves, limiting their energy capture efficiency. Unlike conventional designs that rely on complex active control systems to address this mismatch, this study investigates a passive alternative based on inverted cone-shaped submerged structures that entrap seawater during upward motion, thereby increasing the effective added mass, lowering the natural frequency, and enabling resonance tuning of a roll-based WEC. Building on previous numerical validation, we present results from tests on a 1:40-scale model in regular and irregular waves. Five configurations with varying cone size and suspension distance were evaluated under regular wave excitation. The configuration achieving the highest performance reached a maximum Capture Width Ratio (CWR) of 52%, exceeding the 20%–40% range typical of conventional WECs. To assess robustness under realistic conditions, that configuration was further tested in irregular wave spectra representative of swell-dominated seas. Even under random excitation, the tuned device maintained efficiencies above 20%, demonstrating robustness against spectral variability. The experimental results show close agreement with predictions from a linear analytical model and confirm that passive tuning via cone-shaped structures effectively broadens the resonance bandwidth of roll-harvesting WECs. By combining high efficiency, robustness, and structural simplicity, this low-cost, scalable approach addresses a long-standing limitation of WECs and provides a viable pathway toward full-scale deployment with integrated power take-off damping and adaptation to diverse wave climates.

1. Introduction

Ocean energy is increasingly recognized as a critical component of the global transition toward a post-fossil fuel era [1,2]. Only a fraction of its theoretical potential, estimated at more than 900,000 TWh/year, would suffice to meet the current global electricity consumption [3]. Among ocean energy sources, wave energy stands out for its high power density and predictability [4]. Despite thousands of patented harvesting mechanisms and decades of research, few wave energy converter (WEC) concepts have reached the pre-commercial stage [5]. However, commercialization remains hindered by the high Levelized Cost of Energy (LCOE), survivability concerns in harsh sea conditions, and variability of efficiency in variable wave climates.

Among the WECs successfully deployed as demonstrators, oscillating WECs, which convert the wave-induced motion of floating bodies into electrical energy, have shown particular promise [6–8]. Compared to oscillating water columns (OWC) [9–11] and overtopping

* Corresponding author at: ESPOL Polytechnic University, ESPOL, Faculty of Maritime Engineering and Marine Sciences, Km. 30.5 Vía Perimetral, Guayaquil, 090902, Guayas, Ecuador.
E-mail address: rparedes@espol.edu.ec (R.J. Paredes).

https://doi.org/10.1016/j.ecmx.2026.101575
Received 14 June 2025; Received in revised form 12 January 2026; Accepted 14 January 2026
Available online 28 January 2026

devices [12,13], oscillating bodies typically offer greater energy absorption capability. However, their development remains an iterative multidisciplinary process requiring both hydrodynamic optimization and techno-economic evaluation [14,15]. A key challenge in this process is to ensure that WECs operate near resonance with the dominant wave frequencies to maximize energy capture [16]. Yet, as emphasized by Falnes [17], operating in perfect resonance is not always desirable: in irregular seas, devices often operate off-resonance, and deliberate detuning can reduce structural loads and maintenance costs, though at the risk of undermining techno-economic viability. Within this context, point absorbers and other buoyancy-dominated floaters generally have natural frequencies that are too high to resonate with long-period ocean swells, particularly in tropical and subtropical regions. Alternatively, floaters can be sized to better match incoming wave periods, and hybrid WEC concepts can combine multiple degrees of freedom to broaden their bandwidth and increase efficiency [18].

Various tuning strategies have been proposed to address this mismatch. These strategies include additional structural masses [19], partially flooding compartments [20], moving masses [21], negative stiffness phase control [22], latch mechanisms [23], and PTO-based phase control strategies [24]. However, these approaches often introduce significant penalties in terms of system complexity, cost, and reliability. Structural mass increases buoyancy demands and fabrication costs, while active control systems may become impractical in highly variable or stochastic sea states. However, these approaches still require mechanically intensive subsystems and precision-engineered PTOs, which limits scalability for small or modular systems. These limitations are particularly critical in swell-dominated tropical regions, where long-period waves are consistent and extreme events are rare, creating opportunities for simpler and more robust WEC designs [25].

To overcome these barriers, passive tuning strategies have emerged as promising alternatives. These approaches adjust dynamic properties, such as stiffness or inertia, without relying on active control systems or substantial additional mass. Several point-absorber WEC concepts have demonstrated promising performance, when including tuning devices, based on model scale testing. Tuned inerters can change within a limited range the natural frequency of a Point Absorber (PA) and increase its performance by approximately 40% [26–28]. Likewise, Cai et al. concluded that it is possible to use double-mass pendulums to achieve ultra-low frequencies like those of swells [29]. In addition, yo-yo-like energy harvesters with variable moment of inertia can be used to vary the natural frequency of a WEC in about 11% [30]. This inertia can also be increased for rotary PTOs [31]. Finally, submerged bodies can also be attached to the main floater to increase the efficiency of energy capture [32]. However, these efforts have mainly targeted heave motion, such as the “Wavebob” device, which uses relative acceleration between both bodies to compute inertial forces and then mechanical power [33]. Apart from WEC concepts described above, applications to exploit other degrees of freedom, such as roll or surge, are more limited.

Surge-based converters, such as Oscillating Wave Surge Converters (OWSCs), can theoretically double the maximum capture width due to their asymmetric far-field radiation patterns [34]. Building on this advantage, Mi et al. [35] recently enhanced a surge-tuned OWSC by employing an above-water PTO with a belt arc speed-amplification mechanism, which simplifies the mechanical design while underscoring the efficiency gains attainable through passive or semi-passive surge resonance. However, existing designs have yet to fully exploit roll and pitch resonance, leaving substantial untapped potential in these modes.

More broadly, roll- and pitch-based WEC concepts have been largely overlooked, despite their strong excitation under beam and oblique sea states. Alkhabbaz et al. designed a novel hybrid concept that combines the pitch motions of a flap and a raft [18]. The WEC has Capture Width Ratios (CWR) of 29 and 9% for regular and irregular waves respectively. In addition, the Inertial Sea Wave Energy Converter (ISWEC), a commercial-scale WEC that harnesses pitch motion using internal gyroscopic PTOs and control algorithms to maintain resonance [36–39]. It employs two large internal flywheels and can generate up to 260 kW under Mediterranean wave conditions. However, adapting ISWEC to swell-dominated regions, such as those in the tropics, would require even larger and faster flywheels, substantially increasing system cost and the resulting LCOE. This underlines the need for novel WEC concepts with innovative passive tuning principles that are low-cost, scalable, and efficient in swell conditions, while demonstrating technical feasibility and economic viability early in development [15].

Recently, Guachamín-Acero et al. [40] proposed an innovative passive tuning method that can be applied to different WEC concepts. Their approach uses lightweight open-subsea structures that entrap seawater to modify the natural period of the system instead of relying on structural mass. In their full-scale ANSYS-AQWA simulations, viscous damping was added explicitly, and drag plates with torsional springs were introduced to approximate the expected dual-drag behavior of the cones. This tuning method successfully reduced the natural frequency of both a medium-sized roll-harvesting barge and a small heaving floater, with estimated average mechanical power outputs of 178 kW and 73 kW, respectively. Preliminary techno-economic assessments [41] further indicated a long-term LCOE of 260 USD/MWh under Galápagos swell conditions, outperforming local diesel-based generation. Although early numerical and small-scale tests suggested effective resonance tuning and damping enhancement [42], these results remained limited to simulations, and no comprehensive experimental validation has yet been performed to confirm the feasibility of the concept under realistic conditions. This lack of evidence represents a critical gap in the development of passively tuned roll-harvesting WECs.

The present work extends our previous numerical study [40] by providing the first experimental validation of passive resonance tuning using inverted cone-shaped submerged structures. A 1:40 scale model was tested in regular and irregular waves at the Davidson Laboratory following ITTC and MARINET protocols [43,44]. The experiments confirm the predicted mechanism, entrainment of seawater by the suspended cones increases added mass, shifts the roll resonance frequency, and enhances energy capture. By bridging the gap between numerical feasibility and experimental verification, this study establishes the foundation for practical implementation of scalable roll-harvesting WECs in swell-dominated regions.

2. System description and modeling assumptions

In this study, we examine a passively tuned roll-based WEC as a proof of concept through scale-model experiments and simplified modeling assumptions under controlled laboratory conditions. Guided by a multi-scale concurrent design perspective [45], this section outlines the intended full-scale system architecture, describes the emulated power take-off (PTO) concept at model scale, and clarifies the assumptions used to reduce the inherently multi-body dynamics to a single degree of freedom. This organization situates the experimental campaign within the broader pathway toward practical deployment.

2.1. Full-scale device architecture

The Adaptive Wave Energy Converter (ADWEC) captures ocean wave energy through the roll motion of a passively tuned floating barge and converts it into electrical power for coastal or island applications. As illustrated in Fig. 1, the system comprises two subsystems connected by pulleys and cables: (i) a floating barge with an onboard power take-off (PTO) and electricity generation system, and (ii) a pair of suspended hollow cones, one on each side of the barge, whose differential tension drives the PTO. As wave crests approach from the side, the cones move vertically with the barge’s roll motion, producing asymmetric cable tensions that actuate the PTO and, ultimately, generate electricity.

Passive tuning is achieved by entrapping seawater in the submerged cones, which increases the effective roll inertia and virtual mass of

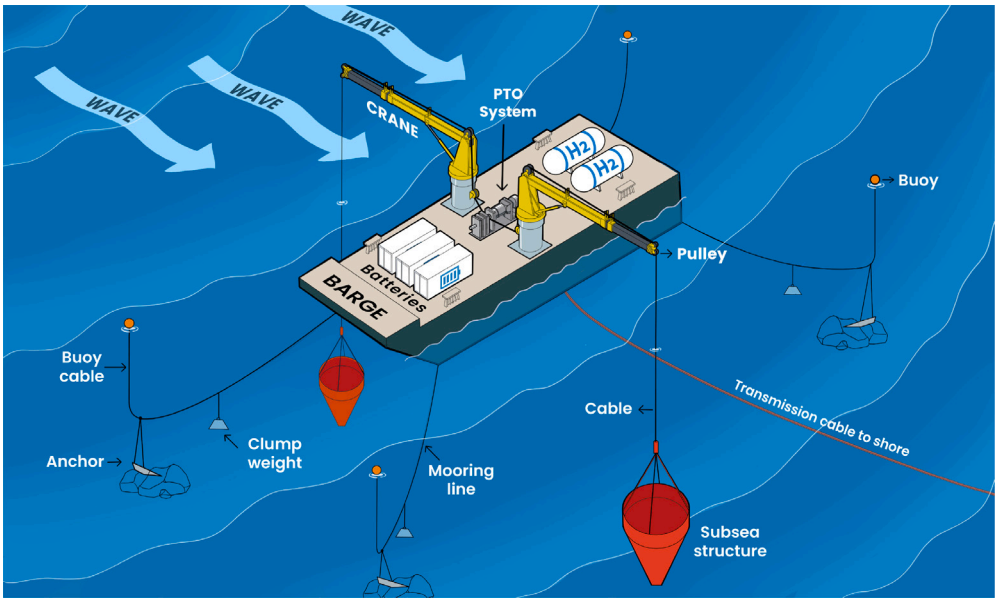

Fig. 1. Conceptual full-scale representation of the Adaptive Wave Energy Converter with Passive Tuning (ADWEC), illustrating its main components and operational context, including electricity conversion and export pathways.

the system. This shifts the natural roll period of the WEC closer to that of swell-dominated seas without requiring additional structural ballast. The conical geometry also reduces downward drag, maintaining cable tautness and enabling a lightweight, structurally simple design. These effects enhance resonance tuning, but the tuners also introduce nonlinear damping that may reduce response amplitude at resonance.

For deployment, the device operates under beam seas, where roll excitation is maximized. A mooring system would maintain heading control by restraining surge, sway, and yaw, while allowing roll motion to dominate. Some misalignment with the incoming wave direction is inevitable, but energy capture is expected to persist as long as the heading offset remains moderate. This orientation requirement is comparable to other WEC concepts that rely on directional resonance.

Despite its simplicity, the design has several limitations. Structural loads at the suspension points may lead to fatigue, while scaling cone size relative to the barge involves trade-offs between efficiency and structural demands. Performance robustness is also influenced by sea-state variability, motivating further work on adaptive geometries and integrated PTO damping. Deployment strategy further shapes applicability: nearshore installations could export electricity directly to the grid, whereas offshore applications may favor conversion to energy carriers such as hydrogen or integration with floating battery storage.

In this work, the experimental model was mounted on a towing carriage that constrained all rigid-body motions except roll. This configuration was intentionally adopted to isolate the roll degree of freedom and provide a proof-of-concept validation of the passive tuning mechanism. While coupling between roll, heave, and pitch will certainly influence the full-scale response, the same model and setup can be extended in future work to investigate these effects and quantify their impact on energy harvesting performance.

2.2. Power Take-Off (PTO) options and idealized emulator

At full scale, energy conversion in the ADWEC system involves three sequential stages: (i) mechanical extraction from wave-induced roll motion, (ii) mechanical-to-electrical conversion, and (iii) electrical conditioning [4]. In the first stage, the barge's roll response, amplified by the inertial reaction of the submerged cones, generates a differential tension in the suspension cables. This tension difference drives a mechanical transmission system that converts cable motion into rotational motion. The oscillatory shaft rotation is then stepped up to over 500 rpm through a bidirectional gearbox, which in turn drives a rotary generator to produce alternating current. Finally, the generated electricity is rectified, inverted, and regulated for grid connection [46], battery storage, or conversion to hydrogen or fresh water.

Several full-scale PTO architectures can be driven by differential cable tension, each offering specific advantages and trade-offs [47]. Hydraulic PTOs [48] convert relative cone–barge motion into high-pressure fluid to power a hydraulic motor–generator set. They can accommodate large loads and provide controllable damping, but introduce additional weight, operational complexity, and conversion losses. Linear direct-drive systems, based on mechanical linkages such as ball screws or rack-and-pinion arrangements [49,50], or on electromagnetic actuators [51,52], minimize moving parts but require large stroke lengths and are generally heavy and costly for roll-based applications. Flywheel-based rotary systems with clutches [53] can smooth oscillatory input but add rotational inertia and raise durability concerns. Among these options, a cable-driven winch configuration (winch–gearbox–generator), which employs a compliant or "soft" connection as proposed by [54,55], aligns naturally with roll excitation, avoids stroke limitations, and relies on mature rotary machinery. This configuration therefore serves as the reference full-scale PTO architecture for ADWEC. A conceptual schematic of this envisioned energy-conversion pathway is shown in Fig. 2, highlighting the transfer of energy from differential cable tension to electrical power.

Implementing any of these PTO architectures at a 1:40 scale is impractical, as miniaturized gearboxes, generators, or hydraulic modules would introduce disproportionate friction, inertia, and conversion losses [56]. As is common in proof-of-concept hydrodynamic testing, a non-intrusive PTO emulator was therefore adopted. Mechanical power was indirectly estimated from the measured cable tensions and roll velocities, which represent the same physical quantities that will ultimately actuate the PTO at full scale. This approach provides a reliable upper-bound estimate of the available mechanical power while preserving the undisturbed hydrodynamic behavior of the model. Future work will focus on developing and testing a scaled physical PTO emulator.

In this formulation, the instantaneous harvested mechanical power is expressed as

$$P(t) = \left[T_2(t) - T_1(t)\right] r_{\mathrm{str}}\, \dot{\phi}(t), \tag{1}$$

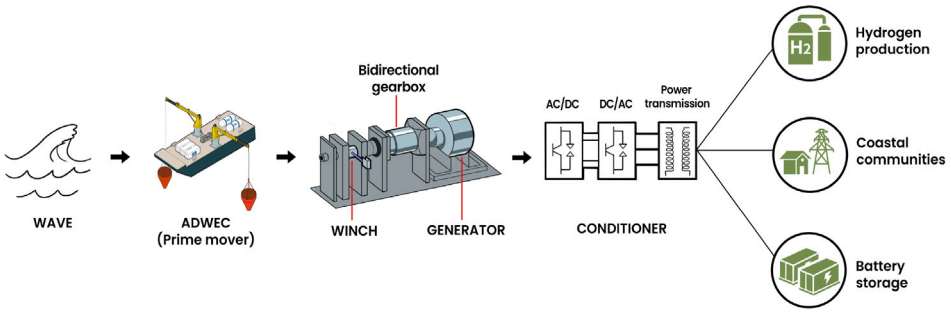

Fig. 2. Conceptual schematic of the envisioned ADWEC power take-off system, illustrating the winch–gearbox–generator energy conversion pathway.

where $T_1(t)$ and $T_2(t)$ are the tensions in the port and starboard cables, respectively, r_{str} is the effective lever arm from the roll axis to the cable attachment point, and $\dot{\phi}(t)$ is the barge's roll angular velocity.

The emulator assumes ideal, lossless conversion and neglects cable elasticity, hysteresis, and generator or gearbox inefficiencies. It also omits relative cone–barge motion and the dynamic feedback associated with PTO-induced damping. These effects are revisited in Section 3.4.3 when discussing harvested power and energy efficiency. Accordingly, the results reported here represent optimistic upper bounds on mechanical energy extraction. More detailed coupled analyses and physical PTO prototypes are planned to quantify these interactions and evaluate realistic power performance.

2.3. Modeling framework and assumptions

The Adaptive Wave Energy Converter (ADWEC) is, in principle, a multibody system comprising the floating barge, two submerged cones, and the suspension slings that connect them. A complete representation would require coupled equations of motion with six degrees of freedom for each body, including nonlinear hydrodynamic and coupling terms. For this proof-of-concept study, the problem is reduced to a single degree-of-freedom (1-DOF) roll model. This choice is justified by the beam-sea configuration described above, where roll dominates the response and cone motions are follow through taut cables. The hydrodynamic influence of the cones is incorporated indirectly via effective added mass, damping, and restoring moment coefficients in the barge's roll equation. This provides a tractable framework while retaining the essential physics of resonance tuning.

This reduction relies on several simplifying assumptions. Roll amplitudes are considered small enough to permit linearization about equilibrium. The cones are assumed identical and symmetrically arranged, although their conical geometry produces asymmetric drag, smaller during the downstroke than the upstroke, an effect lumped into the effective damping term. The suspension slings are assumed taut at all times, preventing slack–snap events and ensuring direct coupling of cone heave to barge roll. Coupling to other rigid-body modes (sway, surge, heave, pitch, yaw) is neglected. At full scale, a mooring system would restrain horizontal and yaw motions; in the experiments, the towing carriage imposed similar constraints, leaving roll as the primary degree of freedom.

Several limitations of this idealization must be acknowledged. Sling elasticity and hysteresis are not included, and nonlinear hydrostatics from time-varying wetted surfaces are also neglected. Such effects can alter the roll restoring moment and reduce the accuracy of linear predictions at larger amplitudes. Pendulum-like lateral motions of the cones are likewise excluded, even though side-to-side oscillations ("falling leaf" motion) may develop in irregular seas or during large roll responses. Prior studies [57] indicate that asymmetric geometries may reduce, but not fully eliminate, the risk of snap loading in compliant connections. These neglected effects, together with explicit multibody dynamics, will be incorporated in future nonlinear models.

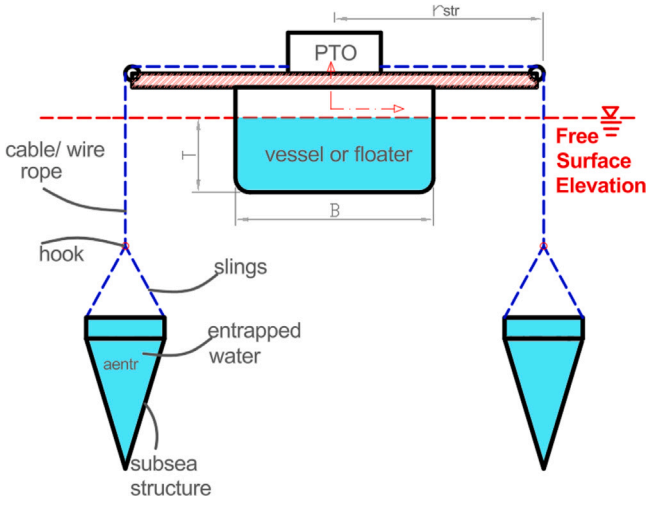

Fig. 3. Simplified 1-DOF model of the Adaptive Wave Energy Converter (ADWEC), where conical-shaped passive tuning devices enable resonance with long-period swells and facilitate roll energy harvesting [40].

In summary, the 1-DOF roll framework provides a simplified yet physically grounded basis for interpreting the experimental results. It clarifies the assumptions and boundaries adopted in this study while establishing a reference point for more comprehensive multibody formulations in future work.

3. Methodology

The following sections describe the linear analytical basis, experimental setup, procedures, and analysis methods used to evaluate the dynamic behavior and energy harvesting performance of the passively tuned roll-based WEC.

3.1. Analytical model of the passively-tuned roll-based WEC

As illustrated in Fig. 3, the roll-based WEC is idealized as a rigid body connected to a pair of submerged conical tuners through taut cables. The entrapped water within the cones provides passive tuning by increasing the roll inertia and virtual mass of the system. This representation reduces the inherently multi-body dynamics into a single-degree-of-freedom roll model, which forms the basis of the analytical formulation.

The uncoupled roll motion of the ADWEC system is then modeled as a linear oscillator under small-amplitude wave excitation. The governing equation is written as:

$$I''_{WEC}\,\ddot{\phi} + B_{44}\,\dot{\phi} + C_{44}\,\phi = F_{EX_4} \tag{2}$$

Here, I''_{WEC} is the effective mass moment of inertia of the entire system, defined as $I''_{barge} + I''_{tuner}$, including contributions from the barge and the tuning devices, respectively. The barge term comprises the dry mass moment of inertia (I_{44}) and the hydrodynamic added mass moment of inertia (A_{44}^{barge}), calculated at its natural frequency. The term B_{44} is the linear roll damping coefficient, and C_{44} is the coefficient of the hydrostatic restoring moment, estimated as $\rho g \nabla GM_T$ for small angles. The angular displacement of the barge is ϕ. Furthermore, ρ is the density of seawater, g is the gravitational acceleration, ∇ is the displacement volume of the barge hull and GM_T is the transverse metacentric height. The excitation moment F_{EX_4} represents the wave-induced torque that excites the roll motion.

The roll natural frequency ω_n of the WEC system is given by:

$$\omega_n = \sqrt{\frac{C_{44}}{I''_{barge} + I''_{tuner}}} \tag{3}$$

The inertial contributions of the barge and the tuning devices are expanded using geometric and hydrodynamic estimates and following Bhattacharyya [58], as follows:

$$\omega_n = \sqrt{\frac{\rho g \nabla GM_T}{k_{44}^2 \rho \nabla + A_{44}^{\text{barge}} + n\, r_{str}^2 (m_{str} + a_{tun} + a_{entr})}} \tag{4}$$

where $k_{44} = 0.35B$ [59] is the dry radius of gyration of the roll.

For each of the tuning devices, m_{str} is their structural mass, a_{tun} is the heave added mass evaluated at the roll natural frequency, a_{entr} is the entrapped seawater mass calculated from the volume of the internal cone, r_{str} is the lateral distance from the barge centerline to the suspension point, and n is the number of tuning structures. The calibrated analytical prediction, based on experimentally derived parameters, is obtained by numerically integrating Eq. (2) using a fourth-order Runge–Kutta method with a fixed time step of 1×10^{-3} s. The numerical integration is initialized with parameters measured from the physical model, including I''_{WEC} and other hydrodynamic properties.

Following [60], the theoretical Response Amplitude Operator (RAO) is calculated assuming that the wave excitation moment is harmonic and proportional to the incident wave amplitude ζ_0 and the effective wave slope, expressed as $k, \zeta_0, r(\omega)$:

$$F_{EX_4} = \Delta GM_T\, k\, \zeta_0\, r(\omega) \tag{5}$$

where k is the wavenumber and $r(\omega)$ is a frequency-dependent correction factor. The RAO is defined as the ratio of the roll amplitude Θ to the wave amplitude:

$$\frac{\Theta}{\zeta_0} = \frac{\Delta\, k\, r(\omega)\, GM_T}{\left| -\omega^2 I''_{WEC} + \Delta GM_T + i\,\omega\, B_{44} \right|} \tag{6}$$

Because this analytical formulation operates in the frequency domain, it predicts response amplitude operators rather than time-domain signals; hence, no direct time-series comparisons were generated. Model validation was instead carried out using RAO curves and free-decay responses, which provide a consistent frequency-based calibration framework. The excitation term follows the IMO wave-slope formulation, assuming harmonic forcing proportional to the incident wave slope and neglecting higher-order nonlinear effects such as quadratic Froude–Krylov and diffraction components. This simplification is adequate for proof-of-concept tests in regular waves but may underestimate excitation at large amplitudes, partly explaining the residual discrepancies between analytical and experimental results. Nonlinear, time-domain simulations incorporating these effects are planned for future work.

3.2. Experimental setup

This section briefly describes the experimental setup of the scaled prototype, including the main characteristics of the device, instrumentation, and the wave tank facility. The experimental campaign was carried out in the wave tank of the Davidson Laboratory at the Stevens Institute of Technology. The effect of the submerged cones, designed to passively shift the natural frequency, on the hydrodynamic performance of the system was evaluated.

3.2.1. The 1:40 WEC physical model

For this experimental proof of concept, a physical model was manufactured following the conceptual WEC design described by Guachamin-Acero et al. [40]. The full-scale system consists of a 1200-ton flat-bottom barge and a passive tuning system using cone-type submerged structures connected with flexible cables. Given the tank dimensions, the WEC model was constructed on a scale of $\lambda = 1/40$ based on Froude similarity.

The hull of the model, shown in Fig. 4, was made of high-density foam. The central volume of the hull was left empty to accommodate a pitch-roll pivot box and ballast weights. The vertical position of the center of gravity (VCG) was experimentally estimated. Six spacers were added under the pivot box to align the roll center of rotation with the estimated VCG. The pivot system was used to measure the corresponding roll angle. Each side of the barge featured an L-shaped beam, made of 8020 aluminum extrusions, mounted mid-length to support the suspended tuning devices. The two support structures were connected with transverse beams at deck level to increase structural rigidity.

Fig. 5 shows a schematic of the three-section tuning devices used in this work. Two cone geometries of different sizes were tested, as summarized in Table 1. Each device was 3D printed with PLA filament and had a wall thickness of 4 mm. A long bolt with nuts and a cap served as the latching mechanism, connecting each cone to the support beams via flexible strings. The total dry weight of the small and large tuning devices was 0.75 kg and 1.08 kg, respectively. The internal volume was designed to entrap 0.86 kg and 3.64 kg of water, respectively. These weights include ballast added to ensure that the flexible string remained taut throughout the tests. The tuning devices were submerged 50 cm to avoid interaction with the free surface.

The physical properties of the WEC model are summarized in Table 1. The roll moment of inertia and the vertical position of the center of gravity (CoG) were experimentally determined by a swing test, following MARINET procedures [61]. For completeness, the corresponding full-scale values from diffraction analysis with ANSYS AQWA, as reported by Guachamín-Acero et al. [40], are also provided. These include the roll added inertia of the barge, A_{44}, and the heave added inertia of the tuning devices, denoted here as a_{tun}. Based on their AQWA simulations of full-scale cones, we adopted a representative relationship of $a_{str} = 0.54\, a_{entr}$, where a_{entr} corresponds to the entrained water mass calculated from the inner volume of the cone. For the barge, A_{44} was also independently approximated using the semi-analytical formulation proposed by Vugts [62].

$$A_{44} = K \rho A_T B^2 L \tag{7}$$

where A_T is the transverse area of the submerged barge section. The coefficient K was taken as 0.093 for the prototype and 0.056 for the model.

The cone dimensions were preliminarily defined using Eq. (4) for the natural roll frequency, together with the hydrodynamic coefficients described above. The small and large cones were then suspended at different transverse spacings constrained by the available arm length. The smaller cones could be placed further outboard, while the larger cones were limited by cable clearance from the barge side. This design strategy allowed exploration of a range of target natural periods approaching the long-period swells typical of the Galápagos, while also capturing the trade-offs between cone size, suspension distance, and structural feasibility.

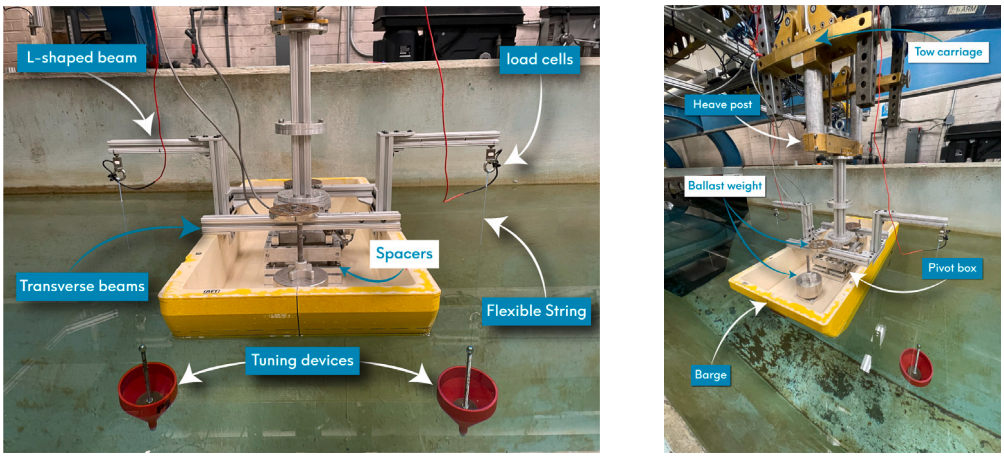

(a) Frontal view (b) Oblique view

Fig. 4. Experimental model of WEC with passive tuning at 1:40 scale installed in the towing tank.

Table 1
Geometrical and inertial properties of the full-scale prototype and 1:40 model. Units in parentheses are given as (prototype/model).

Barge				
Parameter	Symbol	Prototype [40]	1:40 Experimental model	
Length (m/cm)	L	30	80	
Beam (m/cm)	B	14	35	
Draft (m/cm)	T	2.6	7.7	
Mass (tons/kg)	M	1200	18.27	
Vertical position of CoG (m/cm)	VCG	3.5	10.3	
Metacentric height (m/cm)	GM_T	3.5	8.4	
Roll restoring coefficient (N m/rad)	C_{44}	4.1×10^7	15.04	
Roll radius of gyration (m/cm)	k_{44}	4.90	9.3	
Roll moment of inertia (kg m^2)	I_{44}	2.8×10^7	0.1570	
Added mass moment of inertia (kg m^2)	A_{44}	2.04×10^7	0.1389	
Roll natural period of barge (s)	T_{n_barge}	6.9	0.881	
Tuning devices (refer to Fig. 5)				
Parameter	Symbol	Prototype [40]	Small cone	Large cone
Diameters (m/cm)	(D_s, D_i)	(9, 0)	(12, 1)	(20, 1)
Heights (m/cm)	(H_1, H_2, H_3)	(3, 8, 0)	(4, 10, 2)	(6, 16, 2)
Submerged mass (kg)	m_{str}	2.2×10^5	0.75	1.08
Entrapped water mass (kg)	a_{entr}	3.1×10^5	0.86	3.64
Heave added mass	a_{tun}	1.7×10^5	0.466	1.971
Maximum Lever arm (m/cm)	r_{str}	10.0	36.87	27.66
Roll natural period of WEC (s)	$T_{n_{WEC}}$	13.2	1.54	1.90

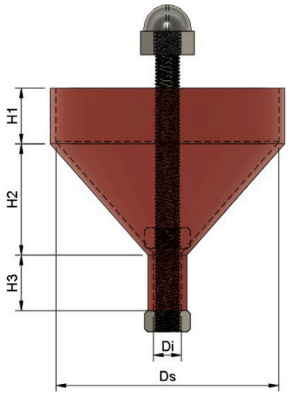

Fig. 5. Schematic showing a schematic of the cone-type tuning device.

3.2.2. Experimental facility

The experiments were carried out in the wave tank of the Davidson Laboratory at Stevens Institute of Technology, shown in Fig. 6. This towing basin measures 95.4 m in length, 4.98 m in width, and 1.97 m in depth. Wave generation and absorption are provided by six "finger-type" paddles, each driven by a Baldor servomotor through a toothed-belt mechanism. The paddles are 1.44 m deep and spaced at 0.83 m intervals, and they can function as both a wave generator and a wave absorber. The wavemaker system can generate regular waves with a frequency range of 0.28 to 2 Hz, wavelengths between 0.5 and 20.0 m, and heights up to 0.60 m. The wavemaker can also generate model sea spectra of any distribution. The average beach absorption efficiency is approximately 94%.

3.2.3. Instrumentation and sensors

The instrumentation consisted of two submersible miniature S-Beam load cells (one per tuning device), model LSB210 with 100 lb capacity, installed between the L-beam structure and the suspension cable to measure dynamic tension; an acoustic wave probe (Senix TS-30S1-IV model) positioned 1.4 m upstream of the model to record the incident wave elevation; and a pitch–roll pivot box instrumented to track the

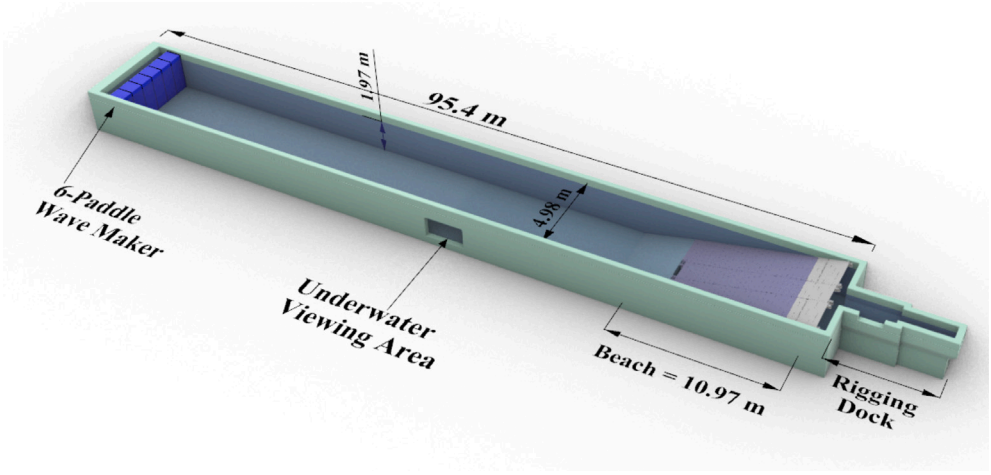

Fig. 6. Davidson laboratory wave tank (95.4 m long) with six-paddle wavemaker, underwater viewing window, and 10.97 m beach.

Table 2
Test matrix.

Parameter	Symbol	Configurations				
		Barge	WEC-C1	WEC-C2	WEC-C3	WEC-C4
Number of tuning devices	n	0	2	2	2	2
Tuning device type		–	smallCone	smallCone	largeCone	largeCone
Lever arm (cm)	r_{str}	–	27.66	36.87	22.58	27.66

roll motion. The roll angle was measured using a mechanical-electrical configuration that included a two-gear system that transmitted the relative rotation to an externally mounted rotary encoder. All signals were acquired at a sampling frequency of 1000 Hz using a synchronized data acquisition system.

The model was attached to the heave post mounted on the tow carriage. Although this setup allows analysis of coupled roll–heave–pitch motion, in this study the model was only allowed to roll freely, while heave, pitch, sway, surge, and yaw were mechanically constrained.

3.3. Experimental procedures

A series of tests were performed to characterize the static stability, natural period, damping, and dynamic roll response of the system. The experiments included inclining tests, free decay tests, and forced oscillations in regular and irregular waves. Each test is described in detail in the following subsections.

3.3.1. Test matrix and WEC configurations

Different configurations of the passively tuned WEC were tested, as shown in Fig. 7 and summarized in Table 2. The baseline configuration was the barge without tuning devices. Configurations WEC-C1 and WEC-C2 employed the small cones, suspended at 27.66 cm (0.79B) and 36.87 cm (1.05B), respectively, corresponding to the maximum available horizontal arm length (8 in from the barge side). These spacings were chosen to shift the natural roll period of the system into the range of 8–10 s at full scale. Since the dominant swell period in the Galápagos is closer to 13 s, larger cones were introduced. WEC-C4 used the large cones at the same spacing as WEC-C1 (0.79B), targeting a natural period closer to 13 s within the limits of the wave generator. To complement this, WEC-C3 placed the large cones 2 in closer to the barge side (0.65B), yielding a natural period intermediate between those of WEC-C2 and WEC-C4. This spacing was the minimum feasible distance, as further reduction would have caused cable interference with the barge.

3.3.2. Inclining and free decay tests

For each configuration, inclining tests were performed to estimate the vertical center of gravity (VCG) and the corresponding transverse metacentric height (GM_T), following IMO procedures [63]. The value of GM_T provides a direct measure of roll stability: when GM_T is positive, the body develops a restoring moment that brings it back upright after a small heel, much like a pendulum swinging back toward equilibrium. If GM_T were negative, the body would be unstable and continue to roll over.

Free decay tests were conducted to estimate the roll natural period, virtual inertia, and linear damping ratio. The barge was manually inclined in roll and released, and the resulting roll motion time series was recorded. Each test was repeated three times per side, using initial roll angles between 6 and 10 degrees, to ensure motion remained within the linear regime. A typical decay curve for the barge configuration is shown in Fig. 8.

3.3.3. Regular waves tests

Regular wave tests were conducted for all configurations to characterize the system response across a range of wave frequencies. Waves were generated over a frequency range between 0.4 and 1.4 Hz with small wave slopes, as shown in Table 3, to avoid nonlinear behavior. The wave slope was gradually increased with frequency to prevent the generation of ripple-like waves as the wavelength decreased. From the Froude similarity law, the full-scale wave environment corresponds to amplitudes between 20 and 60 cm and periods between 4.5 and 15 s. Furthermore, the tuning strategy was designed to achieve resonance at periods exceeding 1.25 s (8 s at full scale), consistent with swell-dominated tropical regions.

The roll RAO provides a direct comparison of the experimental response and the analytical predictions computed using Eq. (6), calibrated using virtual inertia and damping coefficients estimated from free decay tests. The procedure for extracting roll amplitudes and associated uncertainties from the experimental time series is described

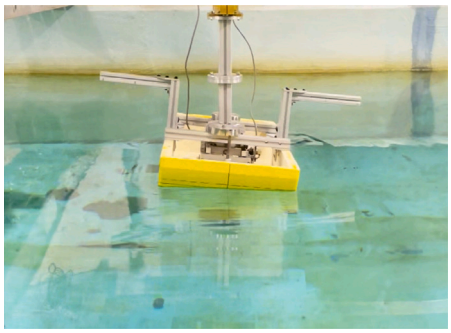

(a) Barge including supporting structure

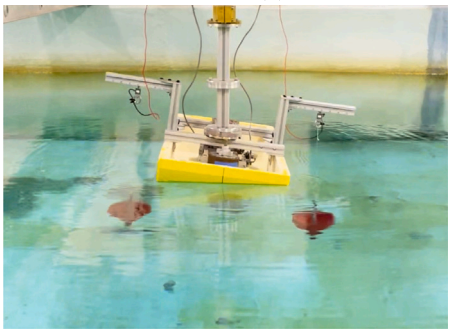

(b) WEC-C1: Barge and small tuning device hanging at 27.66 cm

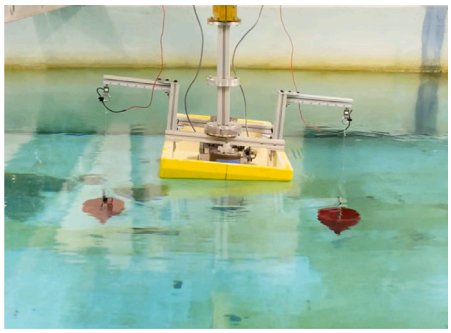

(c) WEC-C2: Barge and small tuning device hanging at 36.87 cm

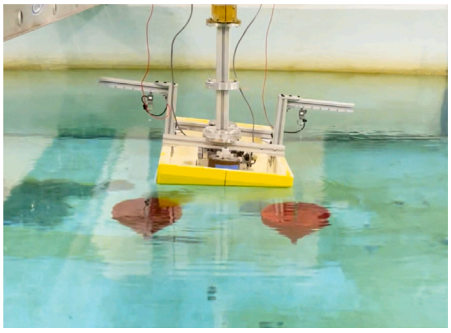

(d) WEC-C3: Barge and large tuning device hanging at 22.58 cm

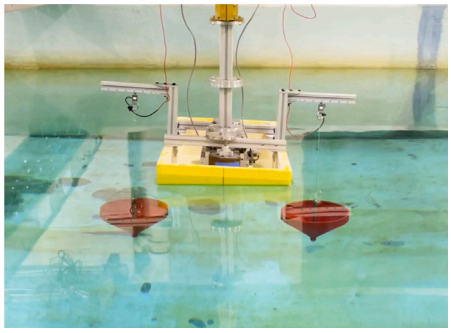

(e) WEC-C4: Barge and large tuning device hanging at 27.66 cm

Fig. 7. Pictures of different experimental setup configurations.

Table 3
Regular wave characteristics used in the present experimental campaign.

Wave frequency f_s [Hz]	Wave period T_w [s]	Wave amplitude ζ_0 [cm]	Wave length L_w [cm]	Wave slope $\frac{2\pi a_0}{L_w}$ [–]	Energy flux P_w [W m^{-1}]
0.4	2.50	1.50	975.82	0.010	2.145
0.5	2.00	1.00	624.52	0.010	0.763
0.6	1.67	1.40	433.70	0.020	1.246
0.7	1.43	1.00	318.63	0.020	0.545
0.8	1.27	1.20	251.82	0.030	0.686
0.9	1.11	0.90	192.75	0.029	0.343
1.0	1.00	0.80	156.13	0.032	0.244
1.1	0.91	0.60	129.03	0.029	0.125
1.2	0.83	0.50	108.42	0.029	0.079
1.3	0.77	0.60	92.39	0.041	0.106
1.4	0.71	0.80	79.66	0.063	0.174

in Section 3.4. The experimental roll RAO was computed using the following:

$$RAO_4 = \frac{\Theta_4}{\zeta_0} \tag{8}$$

where Θ_4 represents the peak amplitude of roll motion and ζ_0 the wave amplitude.

3.3.4. Irregular waves tests

To evaluate the performance of the WEC under realistic random wave conditions, irregular wave tests were conducted. These tests were aimed at validating the roll response and line tension behavior under spectral excitation. Long-crested irregular waves were generated using the ITTC-recommended spectrum [64], which defines the spectral

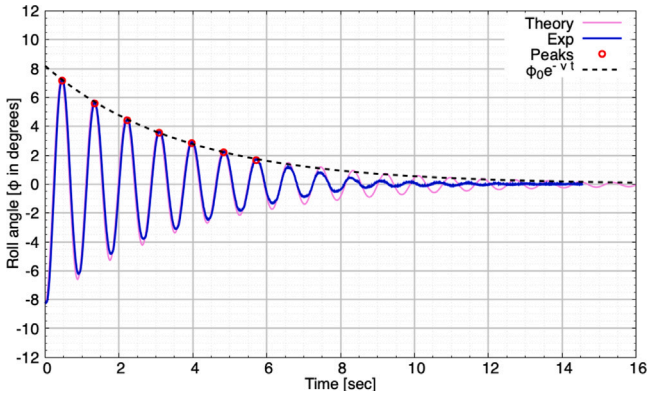

Fig. 8. Typical roll decay curve of the barge-only configuration (Fig. 7(a)).

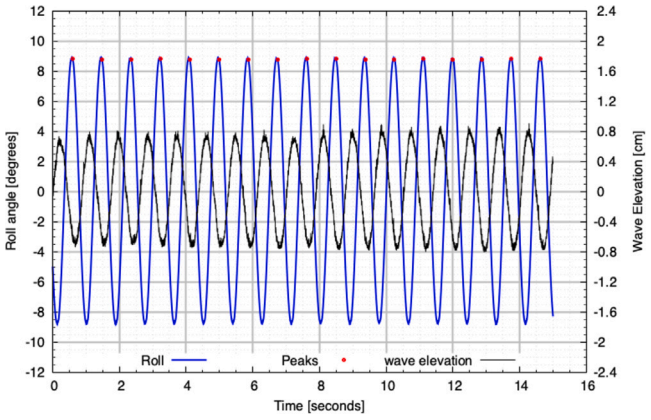

Fig. 9. Experimental results of roll angle time variation for barge configuration during a regular wave test with T = 0.88 s, and a = 6 mm.

energy density $S(f)$, as a function of the significant wave height, H_s and the peak period, T_p:

$$S(f) = \frac{A}{f^5}\exp\left(-\frac{B}{f^4}\right) \tag{9}$$

where f is the wave frequency, $A = 0.0081g^2/K^4$, $B = 4A/H_s^2$. The constant K is defined by the peak period and the significant wave height as $K = (T_p/2.492)\sqrt{g/H_s}$.

Each test was recorded for about 400 s. The first 50 wave cycles (65 s) were discarded to remove startup transients, and the subsequent 210 cycles (270 s) were retained for analysis under steady-state conditions. Time series of roll motion and cable tensions were collected for post-processing and comparison with regular wave performance. Following [35], the wave power per unit length of the crest (wave flux) is estimated as:

$$P_{wave}^{regular} = \frac{\rho g^2}{32\pi}H^2T \tag{10}$$

$$P_{wave}^{irregular} = \frac{\rho g^2}{64\pi}H_s^2T_s \tag{11}$$

where T_s is the wave energy period and H_s is the significant wave height for irregular waves.

In the present wave tank (h = 1.97 m), the resonant operating conditions yield $kh \gtrsim 2.5$. The maximum difference between the deep-water and finite-depth formulations of wave power flux, as given in Newman [65], is 5.8%, observed for the WEC-C4 configuration. For the other resonant conditions, the discrepancy is below 3% and thus negligible. Therefore, we report results using the deep-water formulation for consistency across regular and irregular tests, noting that this choice slightly underestimates wave power and marginally increases the reported CWR values. This effect is well within the experimental uncertainty and does not affect the overall findings.

3.4. Data processing and analysis

This section describes the procedures used to process the experimental data and extract the hydrodynamic and performance characteristics of the WEC system. Time series of roll motion and cable tension were analyzed to determine damping, virtual inertia, roll RAOs, and mechanical power output. Post-processing was performed using MATLAB, including signal smoothing, differentiation, and energy estimation.

3.4.1. Data processing for experiments in waves

Time series of the roll angle were recorded for all wave conditions in each configuration. Fig. 9 shows an example of processed roll angle data for the barge configuration in regular waves (1.14 Hz, 0.60 cm amplitude). Roll amplitudes were obtained by detecting local peaks of the steady-state signal (blue line). From these peaks, both the mean amplitude and the corresponding standard deviation were computed, providing a measure of experimental repeatability. An identical procedure was applied to the incident wave elevation and to the tension-difference forces. The wave elevation (black line) is also shown to illustrate the quality of wave generation.

Using the time-dependent angular displacement, the angular velocity was estimated using the central difference scheme. However, this numerical differentiation introduces high-frequency noise. To reduce this, a moving average filter with a window size of 40 samples is applied, which effectively smoothed the signal while preserving the main dynamic trends and dominant frequency components.

3.4.2. Estimation of hydrodynamic coefficients

Free decay tests were conducted to characterize the fundamental roll dynamics of the system, since they provide a direct means to estimate natural frequencies, damping ratios, and added inertia for floating bodies [66]. Measurements from these tests were analyzed to quantify the hydrodynamic effects of added inertia and damping. The equivalent linear damping ratio, ζ, was estimated using the logarithmic decrement method [67,68], based on two successive amplitude peaks of the roll, positive or negative:

$$\zeta = \sqrt{\frac{ln^2(\phi_{n+2}/\phi_n)}{4\pi^2 + ln^2(\phi_{n+2}/\phi_n)}} \tag{12}$$

Following [69], the roll response of the system is modeled as a damped harmonic oscillator with zero external excitation ($F_{EX_4} = 0$ and $\phi(t=0) = \phi_0$) given by:

$$\phi(t) = \frac{\phi_0}{\sqrt{1-\zeta^2}}e^{-\zeta\omega_n t}sin(\omega_d t + \alpha) \tag{13}$$

where ω_n is the undamped natural frequency and $\omega_d = \sqrt{1-\zeta^2}\omega_n$ is the damped frequency.

The virtual mass moment of inertia of the WEC system, denoted as I''_{WEC}, includes the contributions of both the barge and the tuning devices and is given by:

$$I''_{WEC} = k_{44}^2\rho\nabla + A_{44} \tag{14}$$

Given the known values of the damping ratio ζ, natural frequency ω_n, and metacentric height GM_T, the effective inertia of the system was calculated from the restoring moment using:

$$I''_{WEC} = \frac{\Delta GM_T}{\omega_n^2} \tag{15}$$

The added mass moment of inertia of the WEC system, denoted A_{44}, accounts for the hydrodynamic contributions of the barge and the

tuning devices, and is estimated as

$$A_{44} = \frac{1-\zeta^2}{\omega_d^2}\left(\rho g \nabla G M_T\right) - I_{44} \tag{16}$$

where $I_{44} = \rho \nabla k_{44}^2$ is the dry mass moment of inertia of the barge. Then, the linear roll damping coefficient is estimated as:

$$B_{44} = 2\zeta\left(I_{44} + A_{44}\right)\omega_n \tag{17}$$

These experimentally derived coefficients were then used to interpret RAO responses and support the validation of the passive tuning strategy.

3.4.3. Estimation of harvested mechanical power

Although no PTO system was installed on the barge during the experiments, the differential tension between the cables connected to the submerged tuning devices serves as a proxy for the mechanical input available to an idealized PTO. An idealized PTO system would transform this tension difference into shaft torque through a bidirectional gearbox. The instantaneous harvested mechanical power is therefore evaluated using the formulation introduced in Section 2.2 (Eq. (1)).

The mechanical harvested power at each wave frequency was characterized by the root-mean-square (RMS) of the instantaneous power:

$$P_{WEC}^{\mathrm{RMS}} = \sqrt{\frac{1}{T_{\mathrm{test}}}\int_0^{T_{\mathrm{test}}}\left(P_{WEC}(t)\right)^2 dt}. \tag{18}$$

where T_{test} is the duration of the steady-state window. To quantify variability, the instantaneous power signal was segmented into roll oscillation cycles. For each cycle, the RMS power was calculated, and the standard deviation across all cycles was taken as a measure of experimental repeatability. Reported harvested power values therefore correspond to the global RMS of the power signal, accompanied by the cycle-wise standard deviation.

Device performance is also expressed in nondimensional form through the *Capture Width* (CW) and *Capture Width Ratio* (CWR) [34]. The capture width is defined as the absorbed power normalized by the incident wave power per unit crest length, $CW = P_{WEC}/P_{wave}$. Normalizing by the overall length of the barge L_{OA} yields:

$$CWR = \frac{CW}{L_{OA}} = \frac{P_{WEC}}{P_{wave}\,L_{OA}}, \tag{19}$$

which represents the fraction of the incident wave crest effectively absorbed by the device and it can be interpreted as a nondimensional hydrodynamic efficiency.

To estimate full-scale performance, the Froude scaling laws are applied. Since the angular velocity scales as $\lambda^{0.5}$ and the tension as λ^3, the mechanical power, being the product of force and velocity, scales as:

$$P_{\text{full-scale}} = \lambda^{3.5} P_{WEC}. \tag{20}$$

All power and CWR estimates reported in this study neglect PTO damping. At model scale, the damping ratios of the WEC system, barge, and tuning devices are typically higher due to dominant viscous effects, potentially leading to conservative (underestimated) power predictions. In contrast, omitting PTO-induced damping at full scale may result in overestimated power output. Future work should incorporate both PTO-induced damping and scale-corrected viscous effects to improve the accuracy of full-scale performance estimates.

4. Results and discussion

4.1. Inclining test

The inclining tests were performed to estimate the transverse metacentric height (GM_T) for each configuration. After each weight shift, the system was allowed to settle and the average roll angle was calculated from 30 s of recorded data. To maintain consistent total displacement across configurations, two adjustments were made. First, a part of the fixed ballast was removed in the WEC configurations to compensate for the added wet weight of the suspended tuning devices. This slightly increased the VCG and led to a modest reduction in GM_T. Second, different heeling weights were selected for the tests: 2.0-pound weights for the barge configuration, and lighter weights, 1.2 pounds for small-cone cases and 1.0 pounds for large-cone cases, for the WEC configurations. These adjustments ensured hydrostatically equivalent conditions in all tests. Fig. 10 shows representative results for the barge and WEC-C2 configurations. A linear relationship was observed between the heeling moment and the roll response. The slope of the regression corresponds to the GM_T, and the high values R^2 confirm the consistency of the measurements. Similar behavior was observed in all configurations.

For the barge and WEC configurations, GM_T was calculated from hydrostatic geometry and VCG obtained from inclining tests. The value of KM was 18.6 cm and remained constant across all cases. Variations in VCG due to cone suspension arms were small (a few millimeters) and had negligible effect on overall stability. In particular, increasing the suspension lever arm from WEC-C1 to WEC-C2 led to a small increase in VCG for the small-cone configurations. In contrast, the large-cone cases (WEC-C3 and WEC-C4) exhibited a slight decrease in VCG, likely due to improved vertical mass distribution. These variations remained within a few millimeters and had negligible impact on overall stability. This trend is consistent with expectations. Although the wet weight of the tuning devices is transmitted through the elevated suspension arms, hydrostatic stability is governed by the system's actual mass distribution and waterplane geometry. Since GM_T depends only on the vertical center of gravity and the buoyancy characteristics, it remains unaffected by the height at which loads are transmitted through structural members.

All configurations remained statically stable, with positive values of GM_T. The barge exhibited the highest GM_T (8.5 cm), followed by a gradual decrease as tuning devices were incorporated. These observations confirm that the integration of the tuning structures did not compromise the hydrostatic stability of the platform (see Table 4).

4.2. Free decay test

The hydrodynamic characteristics of the WEC, including its interaction with passive tuning devices, were evaluated through free decay tests. For the Barge, WEC-C1, and WEC-C2, an initial roll angle of approximately 8 degrees was applied, while for WEC-C3 and WEC-C4 the angle was increased to 10 degrees to compensate for the stronger damping introduced by the larger cones. Both values remain within the linear roll regime, ensuring consistency across configurations. Figs. 11 and 12 show the filtered roll response for barge and WEC configurations with small and large cones, respectively. Although the initial amplitudes were comparable, a significant difference in the number of oscillation cycles was evident. This reflects the increased damping and added inertia introduced by the tuning devices.

The inclusion of tuning devices led to a significant increase in the natural period and damping ratio, while the transverse metacentric height remained nearly constant. Within the time window of 4–20 s, the experimental decay curves closely followed the theoretical exponential envelope predicted by Eq. (13), especially for amplitudes larger than 1 degree. This agreement partially supports the validity of the linear model under small-amplitude motion. However, some discrepancies were observed. The calibrated analytical model underestimated the roll amplitudes, and a phase shift was more noticeable in configurations with longer suspension arms. These deviations suggest that linear damping may be insufficient and that a nonlinear damping term could improve the accuracy of the model. Additionally, dynamic coupling effects, such as time-varying tension forces, may contribute to the

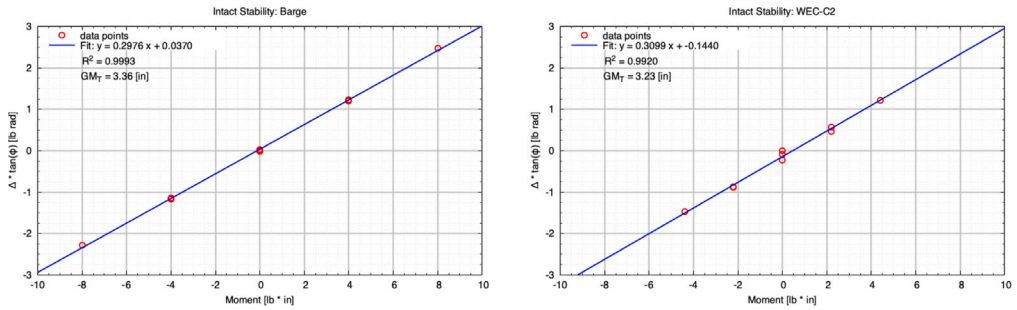

Fig. 10. Inclining test data for barge and WEC-C2 configuration.

Table 4
Summary of metacentric height for all configurations.

Parameter	Symbol	Configurations				
		Barge	WEC-C1	WEC-C2	WEC-C3	WEC-C4
Metacentric height (cm)	GM_T	8.5	8.4	8.2	8.0	8.3
Determination Coeff.	R^2	0.9993	0.9962	0.9920	0.9956	0.9991
Vertical position of CoG (cm)	VCG	10.3	10.4	10.7	10.8	10.6

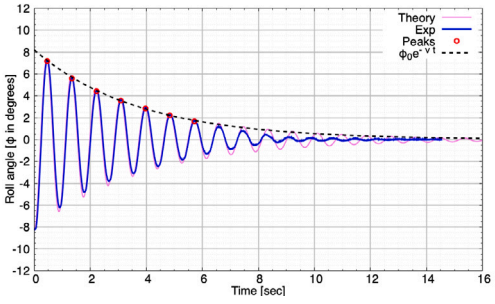

(a) Barge: $T_n = 0.876$ [sec], $\zeta = 0.0377$

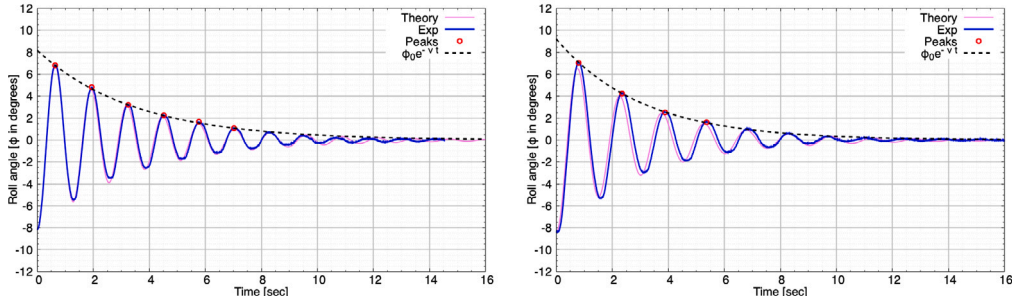

(b) WEC-C1: $T_n = 1.273$ [sec], $\zeta = 0.0583$ (c) WEC-C2: $T_n = 1.498$ [sec], $\zeta = 0.0789$

Fig. 11. Time history of measured roll motion for barge and WEC with small cones configurations (Exp) and selected maximum values (Peaks). The envelope $\phi_0 e^{-\nu t}$ captures the linear damping of free oscillations.

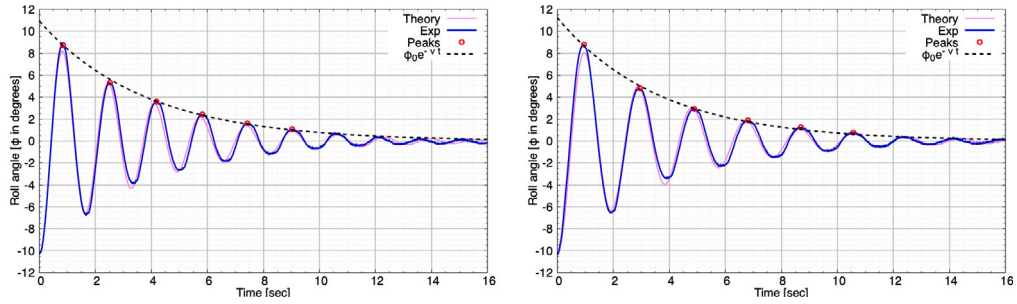

(a) WEC-C3: $T_n = 1.621$ [sec], $\zeta = 0.0681$ (b) WEC-C4: $T_n = 1.917$ [sec], $\zeta = 0.0834$

Fig. 12. Time history of measured roll motion for WEC with large cones configurations (Exp) and selected maximum values (Peaks). The envelope $\phi_0 e^{-\nu t}$ captures the linear damping of free oscillations.

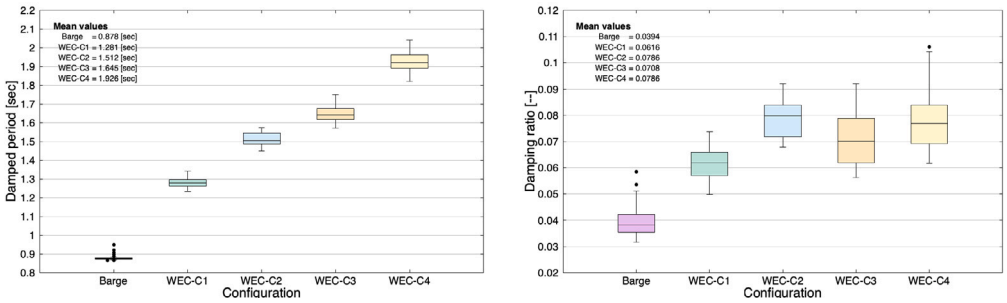

(a) Damped period (b) Damping ratio

Fig. 13. Boxplot of damped period and damping ratio for each configuration. The box in the boxplot spans the range of values from the first quartile to the third quartile of the data points. The crossbar inside each box indicates its median. The whiskers extend from each end of the box for a range equal to 1.5 times the interquartile range. Points shows outlier that lie outside the range of the whiskers.

observed behavior and should be integrated into the restoration term in future modeling efforts.

Fig. 13 presents a boxplot where each data point corresponds to a pair of consecutive peaks (positive or negative) from the six free decay tests conducted for each configuration. The damped natural period increased from 0.88 s (barge) to 1.28 and 1.51 s for WEC-C1 and WEC-C2, and further to 1.64 and 1.92 s for WEC-C3 and WEC-C4. The damping ratio increased accordingly from 0.039 (barge) to approximately 0.062 and 0.079 for the small cones and up to 0.071 and 0.079 for the large cones. These trends reflect the combined effects of the entrapped water and the added mass introduced by the tuning devices. Large-cone configurations achieved longer periods and higher damping ratios, suggesting that future improvements in cone hydrodynamics, such as reducing form drag, may further enhance performance. The wider interquartile ranges in the WEC cases highlight increased variability, reflecting complex nonlinear dynamics introduced by the suspended structures. These variations are attributed to entrapped water mass, added inertia, and the suspension lever arm, all of which amplify the variation of the dynamic response.

Table 5 summarizes the effect of the tuning devices on key dynamic parameters. The virtual moment of inertia and the damping coefficient increased substantially in all WEC configurations. Specifically, damping was roughly doubled with small cones and tripled with large cones. These changes are attributed to two main factors: (1) the larger horizontal projected area of the cones increases viscous drag and generates higher roll-resisting moments; and (2) a longer suspension lever arm increases the moment arm through which hydrodynamic forces act. The virtual radius of gyration also increased with the tuning devices, confirming that the added structures alter the effective mass distribution of the system and the resistance to angular acceleration. This added mass also induces tension in the cables, which directly drives the PTO system. These findings show that large-cone configurations were the most effective in modifying roll characteristics.

The analytical model underestimated the natural period by less than 3% in all cases, indicating that the linear formulation offers a useful first-order approximation. However, it does not fully capture the nonlinear behavior introduced by the tuning devices. As noted by Rusch et al. [57], conical and asymmetric heave-plate structures can exhibit phase-dependent variations in added inertia and damping due to vortex shedding and differences between upstroke and downstroke motion. Within a linear framework, these effects are collapsed into a single effective added inertia coefficient, but future refinements should incorporate their phase dependence to improve predictive fidelity.

4.3. Roll response in regular waves

The RAO was calculated to evaluate the dynamic performance of the different WEC configurations under a wide range of regular wave conditions, providing a direct comparison between experimental results and analytical predictions from the calibrated linear model. At resonance, the tuned WECs exhibited noticeably larger angular displacements compared to the barge, consistent with the frequency-shifting effect of the cones. In the WEC-C1 case, the barge showed the most pronounced roll motion, while the suspended cones introduced slight lateral movements not captured by the analytical model, which is limited to pure roll dynamics. These secondary motions are expected to have negligible influence on the PTO-relevant forces but highlight nonlinear effects introduced by the tuning devices.

The RAO curves, expressed in degrees per centimeter, are plotted against wave frequency in Figs. 14 and 15 for the small- and large-cone configurations, respectively. The results show that the addition of tuning devices shifts the resonant frequency to lower values, corresponding to longer wave periods. This shift is accompanied by a reduction in peak amplitude, consistent with increased damping. The effect is more pronounced in the large-cone configurations, as shown in Fig. 15. The experimental uncertainty is generally small, with narrow $\pm 3\sigma$ bands around the mean curves.

For the barge and small-cone cases (WEC-C1 and WEC-C2), the linear roll model calibrated from free-decay tests reproduces the resonance frequencies well (1.10, 0.78, 0.65 Hz) and captures the overall RAO trends. However, it consistently overpredicts roll amplitudes. This discrepancy arises from two main sources: (i) nonlinear damping mechanisms such as vortex shedding and viscous drag, which are not considered in the linear calibration, and (ii) the simplified excitation formulation. The incident wave moment is modeled following the IMO approach, as harmonic and proportional to the incident wave slope (Eq. (5)), neglecting diffraction and radiation effects. In this case, the barge shows comparatively larger variability near resonance, reflected in more visible uncertainty bands.

For the large-cone configurations (WEC-C3 and WEC-C4), the model again predicts the resonance frequencies but underestimates overall energy dissipation. The larger cones increase added mass while also introducing stronger nonlinear damping from flow separation and vortex shedding, which are not represented in the current linear framework. In addition, the restoring moment is linearized, neglecting the amplitude-dependent effects that reduce stiffness at larger roll angles. Together, these unmodeled effects explain the systematic differences between the semi-analytical predictions and the experimental measurements. As in small-cone cases, the associated uncertainty remains low, and the $\pm 3\sigma$ bands are barely visible.

Fig. 16 shows the RAO of the difference in dynamic tension between the cables, defined as the mean peak force normalized by the mean wave amplitude, plotted against the wave frequency, with shaded bands representing $\pm 3\sigma$ from the distribution of peak values. These curves offer insight into the mechanical energy available for PTO extraction. For the small cone configurations (Fig. 16(a)), the tension RAO closely mirrors the roll RAO, with each setup exhibiting a primary

Table 5
Summary of damped natural period, damping coefficient for all configurations.

Parameter	Symbol	Configurations				
		Barge	WEC-C1	WEC-C2	WEC-C3	WEC-C4
Virtual moment of inertia (kg m^2)	I_{44}	0.297	0.623	0.845	0.977	1.388
Virtual gyroradius ratio	k_{44}/B	0.364	0.528	0.614	0.661	0.787
Virtual added moment of inertia (kg m^2)	A''_{44}	0.140	0.466	0.688	0.820	1.231
Linear damping coefficient (N ms)	B_{44}	0.1675	0.3771	0.5538	0.5298	0.7140
Restoring moment (kg m/rad)	C_{44}	1.553	1.535	1.498	1.462	1.517
Damped Natural frequency (rad/s)	ω_d	7.156	4.905	4.156	3.820	3.262
Natural period (s)						
Theory (Eq. (4))		0.882	1.280	1.544	1.656	1.899
Experiments		0.877	1.279	1.507	1.641	1.920
T-E Difference (%)	(E-T)/E	−0.58	−0.05	−2.43	−0.91	1.07
Damping coefficient						
Number of points	N_{peaks}	70	58	51	63	56
Average	ζ_{exp}	0.0394	0.0616	0.0786	0.0708	0.0786
Variation coeff. (%)	σ/ξ_{exp}	12.9	9.6	8.7	13.6	13.9

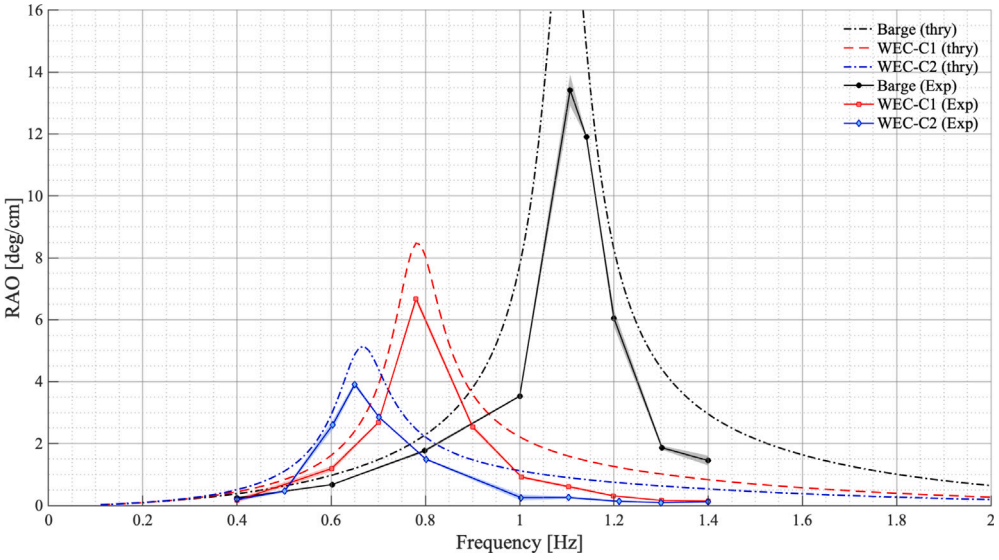

Fig. 14. Roll RAO comparison for barge and WEC with small cones configurations. Shaded regions indicate $\pm 3\sigma$ uncertainty around the experimental mean values.

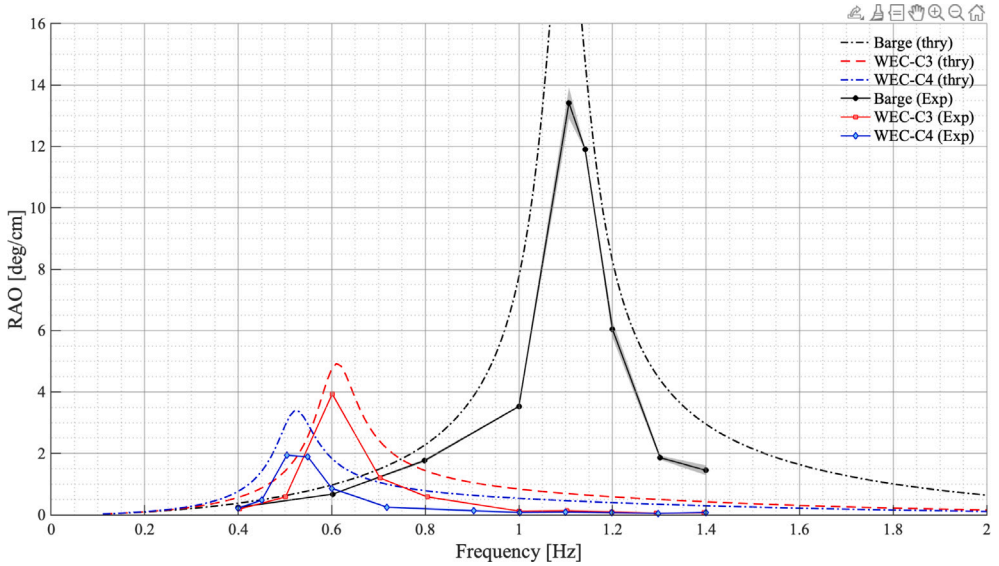

Fig. 15. Roll RAO comparison for WEC with large cones configurations. Shaded regions indicate $\pm 3\sigma$ uncertainty around the experimental mean values.

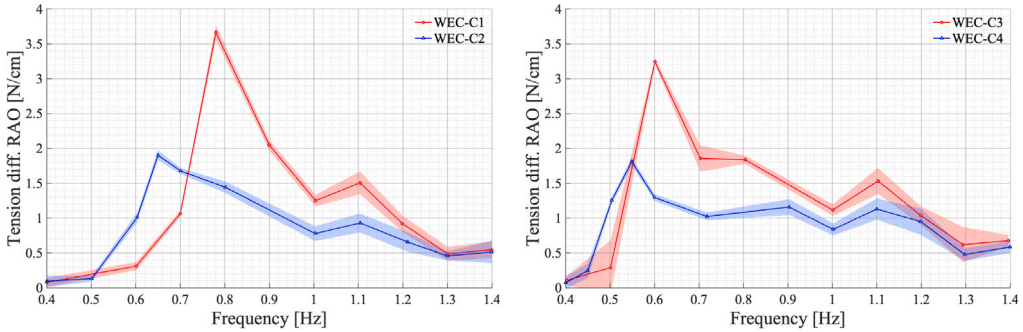

(a) WEC with small cones: WEC-C1 (red) and WEC-C2 (blue) configurations.

(b) WEC with large cones: WEC-C3 (red) and WEC-C4 (blue) configurations.

Fig. 16. Dynamic tension difference RAO for the WEC configurations. Shaded regions indicate $\pm 3\sigma$ uncertainty around the experimental mean values.

resonance peak. In particular, the peak tension for WEC-C1 is approximately 95% greater than that of WEC-C2. Both configurations also exhibit a secondary peak around 1.1 Hz, which may be related to the vibration modes inherent to the cones. The large-cone configurations (Fig. 16(b)) display a similar pattern, although the secondary peaks are broader. This broadening may result from enhanced hydrodynamic coupling or the excitation of multiple cone vibration modes, a phenomenon that warrants further investigation. The associated uncertainty bands are more visible than in the roll RAO plots, highlighting the greater variability of force measurements compared to roll angles.

These results confirm that dynamic tension forces are strongly frequency dependent. As demonstrated by Ruch et al. [57], the drag and added mass coefficients of asymmetric submerged bodies vary with the Keulegan–Carpenter (KC) number, which depends on wave frequency, body size, and amplitude. In our WEC configurations, these variations influence both damping and inertia, contributing to the observed shifts and broadening of tension peaks, particularly in the large-cone cases. Future work should aim to capture these nonlinear, frequency-dependent hydrodynamic effects to enhance PTO force predictions and optimize energy extraction under realistic sea conditions.

4.4. Harvested power in regular waves

Figs. 17 and 18 show the time histories of roll angle, angular velocity, and dynamic tension difference for the four WEC configurations under resonant conditions. The roll angle (gray line) exhibits a stable, nearly sinusoidal behavior, indicating periodic motion. The angular velocity (dashed red line) is also sinusoidal and approximately 90 degrees out of phase with the roll angle, as expected from basic kinematics. Meanwhile, the dynamic tension difference (blue line) is roughly 180 degrees out of phase with the roll angle, highlighting its role as a restoring force. Among all configurations, WEC-C1 exhibits the highest amplitudes in both the angular velocity and tension difference. In contrast, WEC-C2 and WEC-C4 show noticeable deviations from sinusoidal profiles, particularly near peak values, suggesting reduced energy transfer efficiency in these cases.

The corresponding time series of the harvested power are shown in Fig. 19. Because the instantaneous power is defined as the product of roll angular velocity and tension difference, it oscillates between positive and negative values depending on their phase relationship. Negative values occur when the two are out of phase, reflecting the alternating torque direction as the restoring cone switches between port and starboard each half-cycle. A practical PTO must therefore operate bidirectionally (e.g., through a bidirectional gearbox). Reported values correspond to the RMS power, which remains positive and quantifies the net extractable energy. Among small-cone configurations, WEC-C1 achieves the highest RMS output (0.2846 W), more than double that of WEC-C2 (0.1379 W). This corresponds to hydrodynamic efficiencies relative to the available wave power, expressed as CWR, of 52.2% and 14.1%, respectively, as summarized in Table 6. The large-cone configurations exhibit lower performance. WEC-C3 reaches an RMS power of 0.1189 W, while WEC-C4 achieves only 0.0317 W, approximately one-tenth of the value of WEC-C1. The non-sinusoidal, sawtooth-like profile of WEC-C4 indicates increased nonlinear losses or inefficient energy transmission from the roll motion to the tension cables.

Table 6 summarizes the RMS values of angular velocity, tension difference, harvested power, and estimated wave power. The results reveal a stronger correlation between efficiency and angular velocity than between tension and efficiency, consistent with the velocity-dependent nature of damping-based PTO systems, in which maximum power is extracted as the structure crosses through its equilibrium position [70]. The reported uncertainties in harvested power are relatively small compared to the mean values, reinforcing the reliability of the observed performance trends across configurations. In addition to the experimental model-scale values, deterministic full-scale power estimates were derived using Froude scaling (Eq. (20)). These predictions, shown in the last column of Table 6, are provided without uncertainty to facilitate comparison with other WEC studies at sea scale.

4.5. Harvested power in irregular waves

To assess the broadband performance of the most efficient configuration (WEC-C1 at 0.78 Hz), tests were carried out in irregular waves. Two sea states were considered, with significant wave heights of 2.5 and 4.0 cm, corresponding to full-scale Sea States 3 and 4, representative of typical swells in tropical environments. Fig. 20 shows the time histories of wave elevation, roll angle, and mechanical power output for WEC-C1 under Sea State 3. The roll motion appears smoother than the incident wave elevation, illustrating the low-pass filtering effect of the system. Short intervals of zero power output occur when the wave excitation falls below a threshold, likely due to backlash in the mechanical transmission. This behavior is similar to that observed in OSWEC-type WECs [35].

Table 7 summarizes the performance metrics for WEC-C1 in both sea states. Although the wave power nearly triples from SS3 to SS4, the energy conversion efficiency remains stable at approximately 21%–22%. This indicates that the passive-tuning approach maintains performance under increased excitation amplitudes and more nonlinear sea states, without the need for active control. To explore the full-scale potential of the proposed WEC in tropical regions, we considered wave conditions with peak periods around 8 s and significant wave heights between 1.0 and 1.6 m, scaled equivalents of the irregular sea states tested. These conditions are also characteristic of moderate swell climates observed in regions such as western France, Portugal, central California, the Galápagos Islands, and the central coast of Chile [71]. Based on the

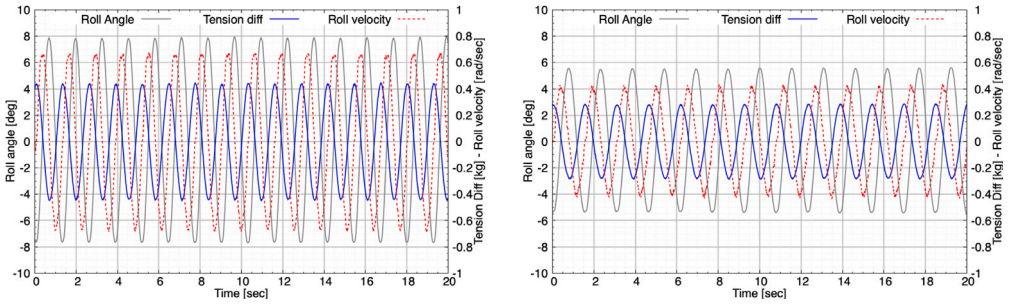

(a) WEC-C1 under 0.78 Hz and 1.17 cm waves. (b) WEC-C2 under 0.65 Hz and 1.43 cm waves.

Fig. 17. Time history of roll angle (gray), angular velocity (dashed red), and dynamic tension difference (blue) for the WEC with small cones. (For interpretation of the references to color in this figure legend, the reader is referred to the web version of this article.)

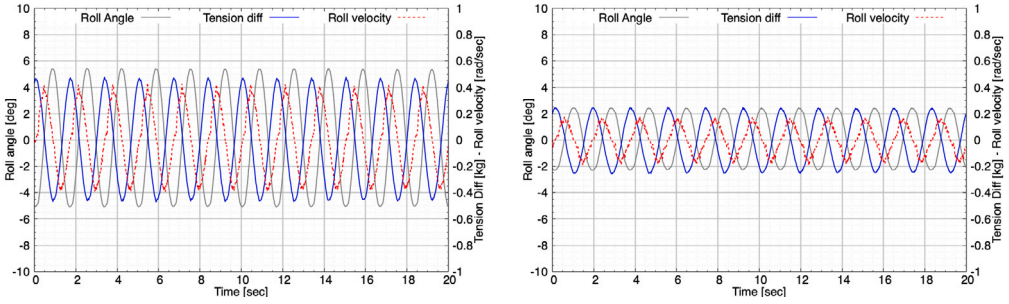

(a) WEC-C3 under 0.60 Hz and 1.39 cm waves. (b) WEC-C4 under 0.55 Hz and 1.29 cm waves.

Fig. 18. Time history of roll angle (gray), angular velocity (dashed red), and dynamic tension difference (blue) for the WEC with large cones. (For interpretation of the references to color in this figure legend, the reader is referred to the web version of this article.)

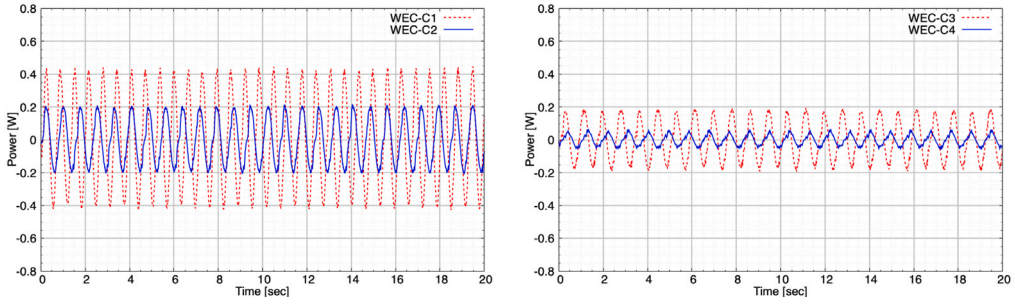

(a) WEC-C1 (dotted red) and WEC-C2 (solid blue).(b) WEC-C3 (dotted red) and WEC-C4 (solid blue).

Fig. 19. Time history of harvested mechanical power for small-cone and large-cone configurations.

Table 6
RMS values of dynamic performance metrics for each configuration under resonant wave conditions.

Config.	Angular velocity (rad/s)	Tension difference (N)	Harvested power (W)	Wave power (W)	CWR Eff. (%)	Full-scale power (kW)
WEC-C1	0.473	3.070	0.2846 ± 0.0018	0.546	52.2	115.20
WEC-C2	0.281	1.944	0.1379 ± 0.0021	0.977	14.1	55.82
WEC-C3	0.249	3.172	0.1189 ± 0.0027	0.994	12.0	48.13
WEC-C4	0.104	1.679	0.0317 ± 0.0019	0.935	3.4	12.83

harvested power measured for the WEC-C1 configuration (Table 7), deterministic full-scale predictions yield mechanical power outputs between 23.8 and 64.4 kW. These values are sufficient to meet basic electricity demands in remote coastal communities or support small-scale applications within the blue economy. Although promising, these projections do not account for scale-induced viscous damping or the dynamic response of a full PTO system. Future work will refine these estimates and investigate strategies to approach the higher efficiencies observed under regular wave conditions.

5. Conclusions

This study presents the first experimental validation of a passively tuned roll-based wave energy converter (WEC) using suspended cone-shaped submerged devices to shift the natural roll period of the system

Table 7
Performance metrics for WEC-C1 configuration in irregular waves.

Sea state	Sig. wave height (cm)	Energy period (s)	Wave power (W)	Harvested power (W)	CWR (%)	Full-scale power (kW)
SS3	2.49	1.144	0.272	0.0589	21.6	23.8
SS4	4.11	1.147	0.741	0.1592	21.5	64.4

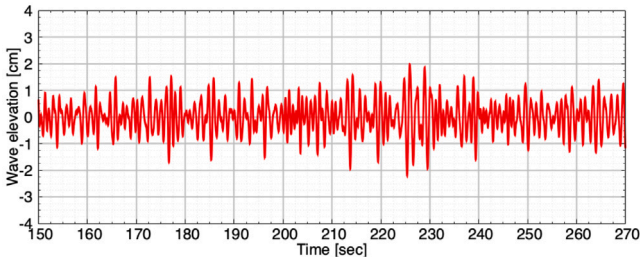

(a) Wave elevation

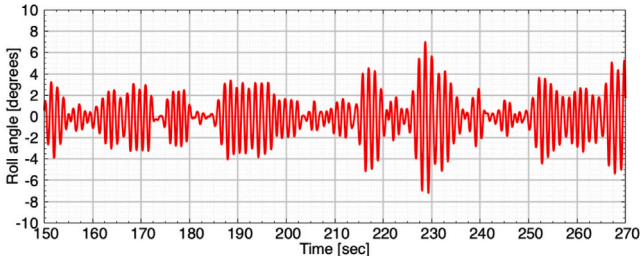

(b) Roll angle

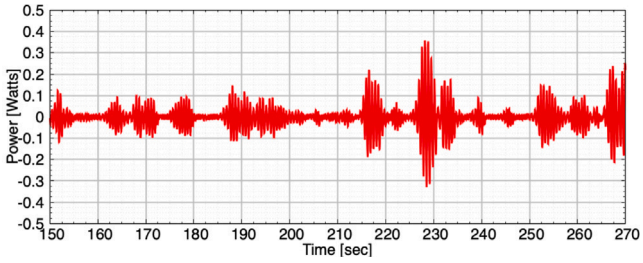

(c) Power harvesting

Fig. 20. Time history of wave elevation (top), roll angle (middle), and power (bottom) for WEC-C1 configurations in Sea State 3, $H_s = 2.5$ cm and $Tp = 1.28$ s.

and improve energy harvesting. A 1:40 scale model was tested under controlled laboratory conditions to assess static stability, roll dynamics, and energy conversion performance in both regular and irregular waves.

Key conclusions are summarized in the following:

- **Resonance tuning:** Passive tuning devices increased the natural roll period of the WEC by up to 2.2 times, allowing resonance with long period swells. The effect scales with the cone geometry, mass, and suspension length.
- **Hydrodynamic damping:** The submerged devices introduced significant damping, up to 2.2 times the bare barge, through increased drag moment and added inertia, without compromising stability.
- **Energy harvesting in regular waves:** The optimal configuration (WEC-C1) achieved 0.285 W at 52% efficiency, exceeding the 20%–40% range typical of conventional WECs. Larger cones traded efficiency for broader frequency adaptability.
- **Performance in irregular waves:** In two swell sea states, WEC-C1 maintained approximately 21.5% efficiency, demonstrating robustness against spectral variability.
- **Analytical model performance:** The calibrated linear model captured general trends but overestimated damping and underestimated peak responses, highlighting the influence of non-linear drag and coupling effects. The present linear model also neglects nonlinear coupling effects such as time-varying wetted surfaces, which may become significant at larger amplitudes.
- **Design optimization potential:** Current results are based on baseline cone geometries and passive damping. Future work will focus on optimizing cone shape, suspension length, and PTO damping to enhance performance.

Beyond these specific findings, the results demonstrate that passive tuning through suspended cones offers a practical pathway to extend the applicability of roll-based WECs to swell-dominated regions such as the Galápagos, where long-period waves prevail and traditional WECs are poorly matched. The ability to achieve efficiencies above 50% in regular waves, with consistently low experimental uncertainties, and to maintain performance robustness under irregular seas, highlights the potential of this concept to deliver reliable energy at scales relevant for island and coastal communities. Unlike active control strategies, this passive tuning method provides a structurally simple, low-maintenance solution that reduces operational complexity and costs. These attributes make the approach well-suited for deployment in remote locations with limited infrastructure, where resilience and simplicity are critical.

This study establishes a foundation for the development of scalable, passively tuned roll-harvesting WECs. A key challenge moving forward is to replicate the high efficiencies observed with WEC-C1 across multiple configurations, while still maintaining adaptability to site-specific wave climates. Future research will therefore focus on (i) refining predictive models to include nonlinear hydrodynamics, tension dynamics, and pitch–heave coupling, (ii) exploring optimized cone shapes and suspension layouts to balance efficiency and bandwidth, and (iii) validating energy capture with a realistic PTO system under moored conditions. Together, these steps will advance the technology toward practical offshore deployment and integration into renewable energy systems for coastal and island communities.

CRediT authorship contribution statement

Ruben J. Paredes: Writing – review & editing, Writing – original draft, Visualization, Validation, Supervision, Methodology, Investigation, Funding acquisition, Formal analysis, Data curation, Conceptualization. **David Plaza:** Writing – original draft, Validation, Investigation, Formal analysis, Data curation. **Raju Datla:** Writing – review & editing, Writing – original draft, Supervision, Methodology, Investigation, Formal analysis, Conceptualization. **Mijail Arias-Hidalgo:** Writing – review & editing, Writing – original draft, Supervision, Methodology, Funding acquisition, Conceptualization. **Paul S. Zambrano:** Writing – original draft, Validation, Software, Investigation. **Jose R. Marin-Lopez:** Writing – review & editing, Writing – original draft, Validation, Methodology, Investigation, Data curation, Conceptualization. **Jose M. Ahumada:** Writing – review & editing, Writing – original draft, Validation, Software, Investigation. **Ricardo Álvarez-Briceño:** Writing – review & editing, Writing – original draft, Validation, Software, Methodology, Investigation, Funding acquisition, Formal analysis, Conceptualization. **Rafael Soria:** Writing – review & editing, Writing – original draft, Validation, Methodology, Investigation, Funding acquisition, Conceptualization. **Wilson Guachamin-Acero:** Writing – review & editing, Writing – original draft, Methodology, Investigation, Funding acquisition, Formal analysis, Conceptualization. **Jesus**

Portilla-Yandun: Writing – review & editing, Writing – original draft, Supervision, Project administration, Methodology, Investigation, Funding acquisition, Formal analysis, Conceptualization. **Muhammad R. Hajj:** Writing – review & editing, Writing – original draft, Resources, Investigation, Conceptualization.

Declaration of competing interest

The authors declare the following financial interests/personal relationships which may be considered as potential competing interests: Jesus Portilla et al. reports financial support was provided by Ecuadorian Corporation for the Development of Research and the Academy (CEDIA). None If there are other authors, they declare that they have no known competing financial interests or personal relationships that could have appeared to influence the work reported in this paper.

Acknowledgments

This work was supported by projects CEDIA I+D+I-XVII-2022-16-WEC GALAPAGOS and EPN-PIGR-2103. The authors thank José A. Barba and Steeven J. Carrión for their contributions to early experimental testing with a 1:100 scale model as part of their capstone design project at ESPOL, which helped anticipate potential challenges. We also acknowledge Myriam Mejía-Herrera for her support with statistical analysis and illustration design. Finally, we are grateful to Christopher "Kip" Francis of Stevens Institute of Technology for his exceptional craftsmanship, which was instrumental to the successful execution of the experimental campaign.

Appendix A. Nomenclature

Roman symbols

Symbol	Description	Unit
GM_T	Transverse metacentric height	m
VCG	Vertical center of gravity	m
B	Beam (breadth of barge)	m
L	Length of barge	m
L_{OA}	Length overall	m
∇	Displacement volume	m^3
$\phi(t)$	Roll angle	rad
$\dot{\phi}(t)$	Roll angular velocity	rad/s
ϕ_0	Initial roll amplitude	rad
$\phi_{\max}$	Peak roll amplitude	rad
I_{44}	Mass moment of inertia (barge)	kg m^2
I''_{WEC}	Virtual inertia of WEC system	kg m^2
I_a, A_{44}	Added mass moment of inertia	kg m^2
B_{44}	Linear damping coefficient	N m s
C_ϕ	Restoring moment coefficient	N m/rad
M_{exc}	Excitation moment	N m
r_{str}	Suspension lever arm	m
H_s	Significant wave height	m
T_p	Peak period	s
T_w	Wave period (regular waves)	s
T_e	Energy period	s
f_s	Wave frequency	Hz
ω	Angular frequency	rad/s
k	Wavenumber	rad/m
a_0	Incident wave amplitude	m
h	Water depth	m
$S(\omega)$	Spectral energy density	m^2/Hz
$P(t)$	Instantaneous harvested power	W
$\overline{P}_{\mathrm{WEC}}$	Mean harvested power	W
P_{rms}	RMS harvested power	W
P_w	Wave power per crest length (regular)	W/m
$P_{w,\mathrm{irr}}$	Wave power per crest length (irregular)	W/m
$P_{w,i}$	Incident wave power per crest length	W/m
P_{fs}	Full-scale harvested power	kW
T	Test duration	s

Greek symbols

Symbol	Description	Unit
ζ	Damping ratio	–
ω_n	Natural frequency	rad/s
ω_d	Damped natural frequency	rad/s
θ	Phase angle	rad
α, γ	Pierson–Moskowitz spectrum constants	–
$\beta(kh)$	Finite-depth correction factor	–
λ	Geometric scale factor	–

Subscripts and superscripts

Symbol	Meaning
p, s	Port and starboard
b	Barge
t	Tuning device
a	Added or apparent
rms	Root-mean-square
fs	Full scale
n	nth cycle

Appendix B. Abbreviations

Acronym	Definition
ADWEC	Adaptive Wave Energy Converter
CoG	Center of Gravity
CW	Capture Width
CWR	Capture Width Ratio
DOF	Degree of Freedom
GM	Metacentric Height
IMO	International Maritime Organization
ISWEC	Inertial Sea Wave Energy Converter
ITTC	International Towing Tank Conference
KC	Keulegan–Carpenter number
LCOE	Levelized Cost of Energy
LOA	Length Overall
MARINET	Marine Renewables Infrastructure Network for Emerging Energy Technologies
OSWEC	Oscillating Surge Wave Energy Converter
OWC	Oscillating Water Column
OWSC	Oscillating Wave Surge Converter
PLA	Polylactic Acid (3D printing filament)
PTO	Power Take-Off
RAO	Response Amplitude Operator
RMS	Root Mean Square
SS	Sea State
VCG	Vertical Center of Gravity
WEC	Wave Energy Converter

Data availability

Data will be made available on request.

References

[1] IEA. World energy outlook 2023. Tech. rep., Paris, France: International Energy Agency; 2023, p. 355, URL https://www.iea.org/reports/world-energy-outlook-2023.

[2] Tapoglou E, Georgakaki A, Letout S, Kuokkanen A, Mountraki A, Ince E, Shtjefni D, Joanny Ordonez G, Eulaerts O, Grabowska M. Ocean energy in the European Union – 2022 status report on technology development, trends, value chains and markets. Luxembourg: Clean Energy Technology Observatory; 2022, p. 78. http://dx.doi.org/10.2760/162254, URL https://publications.jrc.ec.europa.eu/repository/handle/JRC130617.

[3] Krewitt W, Nienhaus K, Kleßmann C, Capone C, Stricker E, Graus W, Hoogwijk M, Supersberger N, Winterfeld Uv, Samadi S. Role and potential of renewable energy and energy efficiency for global energy supply. Clim Chang 2009;18:345, URL http://nbn-resolving.de/urn:nbn:de:kobv:109-opus-83759.

[4] Penalba M, Ringwood JV. A review of wave-to-wire models for wave energy converters. Energies 2016;9(7). http://dx.doi.org/10.3390/en9070506.

[5] de Oliveira L, Santos IFSd, Schmidt NL, Tiago Filho GL, Camacho RGR, Barros RM. Economic feasibility study of ocean wave electricity generation in Brazil. Renew Energy 2021;178:1279–90. http://dx.doi.org/10.1016/j.renene.2021.07.009.

[6] Dalton GJ, Alcorn R, Lewis T. Case study feasibility analysis of the Pelamis wave energy convertor in Ireland, Portugal and North America. Renew Energy 2010;35(2):443–55. http://dx.doi.org/10.1016/j.renene.2009.07.003.

[7] Weber J, Mouwen F, Parish A, Robertson D. Wavebob – Research & development network and tools in the context of systems engineering. In: The 8th European wave and tidal energy conf. EWTEC, Uppsala, Sweden; 2009, p. 416–20.

[8] Energy CC. CETO 5 – Perth (WA). URL https://www.carnegiece.com/portfolio/ceto-5-perth-wa/.

[9] ARENA. Oceanlinx 1MW commercial wave energy demonstrator. URL https://arena.gov.au/projects/oceanlinx-1mw-commercial-wave-energy-demonstrator/.

[10] Falcão AF, Sarmento AJ, Gato LM, Brito-Melo A. The Pico OWC wave power plant: Its lifetime from conception to closure 1986–2018. Appl Ocean Res 2020;98(April):102104. http://dx.doi.org/10.1016/j.apor.2020.102104.

[11] Torre-Enciso Y, Ortubia I, López de Aguileta LI, Marqués J. Mutriku wave power plant: from the thinking out to the reality. In: 8th European wave and tidal energy conference. EWTEC 2009, 2009, p. 319–28, (August), URL http://tethys.pnnl.gov/sites/default/files/publications/Torre-Enciso_et_al_2009.pdf.

[12] Contestabile P, Ferrante V, Di Lauro E, Vicinanza D. Prototype overtopping breakwater for wave energy conversion at port of Naples. In: Proceedings of the international offshore and polar engineering conference. ISOPE, Rhodes, Greece; 2016, p. 616–21, no. July.

[13] PNNL. Wave dragon pre-commercial demonstration project. 2018, URL https://tethys.pnnl.gov/project-sites/wave-dragon-pre-commercial-demonstration-project.

[14] Trueworthy A, Dupont B. The wave energy converter design process: Methods applied in industry and shortcomings of current practices. J Mar Sci Eng 2020;8(11):1–49. http://dx.doi.org/10.3390/jmse8110932.

[15] Weber J. WEC technology readiness and performance matrix – finding the best research technology development trajectory. In: International conference on ocean energy, ICOE. Dublin; 2012, p. 1–10, no. OCTOBER 2012.

[16] Falcão AFO. Wave energy utilization: A review of the technologies. Renew Sustain Energy Rev 2010;14(3):899–918. http://dx.doi.org/10.1016/j.rser.2009.11.003.

[17] Falnes J. Optimum control of oscillation of wave-energy converters. Int J Offshore Polar Eng 2002;(2). URL http://onepetro.org/IJOPE/article-pdf/2181792/isope-02-12-2-147.pdf.

[18] Alkhabbaz A, Hamzah H, Hamdoon OM, Yang HS, Easa H, Lee YH. A unique design of a hybrid wave energy converter. Renew Energy 2025;245. http://dx.doi.org/10.1016/j.renene.2025.122814.

[19] De Backer G, De Rouck J. Hydrodynamic design optimization of wave energy converters consisting of heaving point absorbers [Ph.D. thesis], University Gent; 2009, p. 344, URL http://awww.ugent.behttp//www.maritiem.ugent.be.

[20] Flocard F, Finnigan TD. Increasing power capture of a wave energy device by inertia adjustment. Appl Ocean Res 2012;34:126–34. http://dx.doi.org/10.1016/j.apor.2011.09.003.

[21] Cai Y, Shi X, Huo Y, Liu Y. Experimental study on a pitching wave energy converter with adjustable natural period. Ocean Eng 2022;261. http://dx.doi.org/10.1016/j.oceaneng.2022.112128.

[22] Windt C, Faedo N, Penalba M, Dias F, Ringwood JV. Reactive control of wave energy devices – the modelling paradox. Appl Ocean Res 2021;109(February). http://dx.doi.org/10.1016/j.apor.2021.102574.

[23] Budal K, Falnes J. Wave power conversion by point absorbers: A norwegian project. Int J Ambient Energy 1982;3(2):59–67. http://dx.doi.org/10.1080/01430750.1982.9675829.

[24] Babarit A, Guglielmi M, Clément AH. Declutching control of a wave energy converter. Ocean Eng 2009;36(12–13):1015–24. http://dx.doi.org/10.1016/j.oceaneng.2009.05.006, URL https://linkinghub.elsevier.com/retrieve/pii/S0029801809001115.

[25] Portilla-Yandún J, Acero WG, Soria R, Bravo J, Alvarez R, Paredes R, Arias M. Spectral and entropy-based wave energy resource assessment: A global view, and point analysis at the Galapagos Islands. Renew Energy 2025;246:122830. http://dx.doi.org/10.1016/j.renene.2025.122830, URL https://linkinghub.elsevier.com/retrieve/pii/S0960148125004926.

[26] Sugiura K, Sawada R, Nemoto Y, Haraguchi R, Asai T. Wave flume testing of an oscillating-body wave energy converter with a tuned inerter. Appl Ocean Res 2020;98. http://dx.doi.org/10.1016/j.apor.2020.102127, URL https://linkinghub.elsevier.com/retrieve/pii/S0141118720300201.

[27] Haraguchi R, Asai T. Enhanced power absorption of a point absorber wave energy converter using a tuned inertial mass. Energy 2020;202. http://dx.doi.org/10.1016/j.energy.2020.117740.

[28] Sun T, Zhang Z. Optimal control and performance evaluation of an inerter-based point absorber wave energy converter. Ocean Eng 2022;259(July):111883. http://dx.doi.org/10.1016/j.oceaneng.2022.111883.

[29] Cai Q, Zhu S. Applying double-mass pendulum oscillator with tunable ultra-low frequency in wave energy converters. Appl Energy 2021;298. http://dx.doi.org/10.1016/j.apenergy.2021.117228, URL https://linkinghub.elsevier.com/retrieve/pii/S0306261921006504.

[30] Jang S-J, Kim B-R. Resonant frequency tuning of wave energy converters using variable moment of inertia. J Adv Mar Eng Technol 2023;47(1):12–5. http://dx.doi.org/10.5916/jamet.2023.47.1.12.

[31] Thomas S, Giassi M, Göteman M, Hann M, Ransley E, Isberg J, Engström J. Performance of a direct-driven wave energy point absorber with high inertia rotatory power take-off. Energies 2018;11(9):1–17. http://dx.doi.org/10.3390/en11092332.

[32] Bozzi S, Miquel AM, Antonini A, Passoni G, Archetti R. Modeling of a point absorber for energy conversion in Italian seas. Energies 2013;6(6):3033–51. http://dx.doi.org/10.3390/en6063033.

[33] Tarrant K, Meskell C. Investigation on parametrically excited motions of point absorbers in regular waves. Ocean Eng 2016;111:67–81. http://dx.doi.org/10.1016/j.oceaneng.2015.10.041, URL https://linkinghub.elsevier.com/retrieve/pii/S0029801815005880.

[34] Babarit A. A database of capture width ratio of wave energy converters. Renew Energy 2015;80:610–28. http://dx.doi.org/10.1016/j.renene.2015.02.049, URL https://linkinghub.elsevier.com/retrieve/pii/S0960148115001652.

[35] Mi J, Huang J, Li X, Ahmed A, Yang L, Chung U, Datla R, Hajj M, Zuo L. Oscillating surge wave energy converter using a novel above-water power takeoff with belt-arc speed amplification. Ocean Eng 2024;310. http://dx.doi.org/10.1016/j.oceaneng.2024.118503.

[36] Bracco G, Giorcelli E, Mattiazzo G, Tedeschi E, Molinas M. Control strategies for the ISWEC wave energy system. In: 9th European wave and tidal energy conference. EWTEC11, Southampton, United Kingdom; 2011, p. 1–10, no. November 2014.

[37] Bracco G, Giorcelli E, Giorgi G, Mattiazzo G, Passione B, Raffero M, Vissio G. Performance assessment of the full scale ISWEC system. In: 2015 IEEE international conference on industrial technology. ICIT, vol. 2015-June, Seville, Spain: IEEE; 2015, p. 2499–505. http://dx.doi.org/10.1109/ICIT.2015.7125466, URL http://ieeexplore.ieee.org/document/7125466/.

[38] Sirigu SA, Bonfanti M, Begovic E, Bertorello C, Dafnakis P, Giorgi G, Bracco G, Mattiazzo G. Experimental investigation of the mooring system of a wave energy converter in operating and extreme wave conditions. J Mar Sci Eng 2020;8(3). http://dx.doi.org/10.3390/jmse8030180.

[39] Idrocarburi EN. The installation of ISWEC (inertial sea wave energy converter) off the coast of pantelleria has been completed. 2023, URL https://www.eni.com/en-IT/media/press-release/2023/03/installation-iswec-off-coast-pantelleria-has-been-completed.html.

[40] Guachamin-Acero W, Alvarez R, Segovia J, Salguero M, Bravo J, Paredes R, Arias-Hidalgo M, Soria R, Portilla-Yandún J. Feasibility study of a method for tuning wave energy converters. Sustain Energy Technol Assess 2024;64:103702. http://dx.doi.org/10.1016/j.seta.2024.103702, URL https://linkinghub.elsevier.com/retrieve/pii/S2213138824000985.

[41] Meneses E, Soria R, Portilla J, Guachamín-Acero W, Álvarez R, Paredes R, Arias-Hidalgo M. The potential of wave energy converters in the Galapagos islands. Energy Strategy Rev 2024;54:101457. http://dx.doi.org/10.1016/j.esr.2024.101457, URL https://linkinghub.elsevier.com/retrieve/pii/S2211467X24001640.

[42] Paredes RJ, Plaza D, Arias-Hidalgo M, Marin-Lopez JR, Datla R, Hajj M. Experimental assessment of a roll-based wave energy converter. In: Proceedings of the ASME 2025 44th international conference on ocean, offshore and arctic engineering (OMAE 2025). volume 5: Ocean renewable energy. Vancouver, Canada: American Society of Mechanical Engineers; 2025, http://dx.doi.org/10.1115/OMAE2025-156292, URL https://asmedigitalcollection.asme.org/OMAE/proceedings/OMAE2025/88940/V005T09A052/1221434.

[43] 29th ITTC. ITTC 7.5-02-07-03.7 – Recommended procedures and guidelines: Wave energy converter model test experiments. Tech. rep., Virtual: International Towing Tank Conference (ITTC); 2021, p. 18, URL https://www.ittc.info/media/9745/75-02-07-037.pdf.

[44] Têtu A, Frigaard P, Kofoed JP, Lopes M, Iyer A, Ourdier D, SylvainMarina, Stripling S, Johanning L. D2.5EC report on instrumentation best practice report on instrumentation best practice. Tech. rep., MARINET; 2013.
[45] Mi J, Huang J, Yang L, Ahmed A, Li X, Wu X, Datla R, Staby B, Hajj M, Zuo L. Multi-scale concurrent design of a 100 kW wave energy converter. Renew Energy 2025;238. http://dx.doi.org/10.1016/j.renene.2024.121835.
[46] Ringwood JV, Zhan S, Faedo N. Empowering wave energy with control technology: Possibilities and pitfalls. 2023, http://dx.doi.org/10.1016/j.arcontrol.2023.04.004.
[47] Ulum Arga Pratama Zakaria MF, Mukhtasor. State of the art of Power Take Off (PTO) systems in Wave Energy Converter (WEC). 2025, http://dx.doi.org/10.1016/j.oceaneng.2025.121669.
[48] Jenne S, Panzarella J, Simms A, Muglia M, Raye R, Nichols C, Bharath A, Candon C, Schnabel A, Mcgilton B, Murphy M, Swartz K. HERO WEC V1: Design and experimental data collection efforts. Tech. rep., Golden, CO: National Renewable Energy Laboratory (NREL); 2024, URL https://www.nrel.gov/docs/fy25osti/91741.pdf.
[49] Zhang Y, Huang H, Gao F, Chen W. Cable-driven power take-off for WEC-glider: Modeling, simulation, experimental study, and application. Energy 2023;282. http://dx.doi.org/10.1016/j.energy.2023.128851.
[50] Li X, Chen CA, Li Q, Xu L, Liang C, Ngo K, Parker RG, Zuo L. A compact mechanical power take-off for wave energy converters: Design, analysis, and test verification. Appl Energy 2020;278. http://dx.doi.org/10.1016/j.apenergy.2020.115459.
[51] Li M, Jing X. A bistable X-structured electromagnetic wave energy converter with a novel mechanical-motion-rectifier: Design, analysis, and experimental tests. Energy Convers Manage 2021;244. http://dx.doi.org/10.1016/j.enconman.2021.114466.
[52] Viet NV, Wang Q. Ocean wave energy pitching harvester with a frequency tuning capability. Energy 2018;162:603–17. http://dx.doi.org/10.1016/j.energy.2018.08.067.
[53] Jia H, Pei Z, Tang Z, Li M. Modeling, analysis and control of an inertial wave energy converter and hydraulic power take-off unit. Sci Rep 2025;15(1). http://dx.doi.org/10.1038/s41598-025-91953-6.
[54] Liu M, Bennett A, Ruan F, Li X, Lou J, Mi J, Zuo L. A self-reactive ocean wave energy converter with winch-based power take-off: Design, prototype, and experimental evaluation. In: Volume 10: 34th conference on mechanical vibration and sound. VIB, St. Louis, Missouri: American Society of Mechanical Engineers; 2022, http://dx.doi.org/10.1115/DETC2022-91303, URL https://asmedigitalcollection.asme.org/IDETC-CIE/proceedings/IDETC-CIE2022/86311/V010T10A012/1150699.
[55] Zhang H, Sun L, Liu J, Mi J, Li X, Xu L, Zuo L. Numerical analysis and wave tank test of a point absorber wave energy converter using a tether driven power take-off system. In: Proceedings of the ASME 2023 international design engineering technical conferences and computers and information in engineering conference IDETC/CIE2023. Boston, Massachusetts: SNAME; 2023, http://dx.doi.org/10.1115/DETC2023-114939.
[56] Giannini G, Temiz I, Rosa-Santos P, Shahroozi Z, Ramos V, Göteman M, Engström J, Day S, Taveira-Pinto F. Wave energy converter power take-off system scaling and physical modelling. J Mar Sci Eng 2020;8(9). http://dx.doi.org/10.3390/JMSE8090632.
[57] Rusch CJ, Mundon TR, Maurer BD, Polagye BL. Hydrodynamics of an asymmetric heave plate for a point absorber wave energy converter. Ocean Eng 2020;215. http://dx.doi.org/10.1016/j.oceaneng.2020.107915.
[58] Bhattacharyya R. Dynamics of marine vehicles. Wiley; 1978.
[59] Faltinsen O. Sea loads on ships and offshore structures. Cambridge, UK: Cambridge University Press; 1993, p. 340.
[60] Interim guidelines on the second generation intact stability criteria. Tech. rep., London: International Maritime Organization (IMO); 2020.
[61] Marine Renewables Infrastructure Network. WP2: Marine energy system testing - Standardisation and best practice. D2.28: Model construction methods. Tech. rep., MARINET; 2015, URL www.fp7-marinet.eu.
[62] Vugts JH. The hydrodynamic coefficients for swaying, heaving, and rolling cylinders ina free surface. Tech. rep., Delft: Delft Technological University; 1968, p. 151.
[63] Maritime Organization I. Resolution MSC 267 85: Adoption of the international code on intact stability. Tech. rep., International Maritime Organization (IMO); 2009.
[64] The Specialist committee on Waves. Final report and recommendations to the 23rd ITTC. Tech. rep., International Towing Tank Conference (ITTC); 2002.
[65] Newman JN. Marine hydrodynamics. The MIT Press; 1977, http://dx.doi.org/10.7551/mitpress/4443.001.0001, URL https://direct.mit.edu/books/book/2693/marine-hydrodynamics.
[66] Alkhabbaz A, Hamza H, Daabo AM, Yang HS, Yoon M, Koprulu A, Lee YH. The aero-hydrodynamic interference impact on the NREL 5-MW floating wind turbine experiencing surge motion. Ocean Eng 2024;295. http://dx.doi.org/10.1016/j.oceaneng.2024.116970.
[67] Rao S. Mechanical vibrations. 6th ed.. Pearson; 2016.
[68] Begovic E, Bertorello C, Prpic-Orsic J. Roll damping coefficients assessment and comparison for round bilge and hard chine hullforms. In: Proceedings of the ASME 2013 32nd international conference on ocean, offshore and arctic engineering OMAE2013. Nantes, France: ASME; 2013, p. 1–9. http://dx.doi.org/10.1115/OMAE2013-10620.
[69] Zeraatgar H, Asghari M, Bakhtiari-Nejad F. A study of the roll motion by means of a free decay test. J Offshore Mech Arct Eng 2010;132(3):1–8. http://dx.doi.org/10.1115/1.4000393.
[70] Fusco F, Ringwood JV. A study of the prediction requirements in real-time control of wave energy converters. IEEE Trans Sustain Energy 2012;3(1):176–84. http://dx.doi.org/10.1109/TSTE.2011.2170226.
[71] Young IR. Seasonal variability of the global ocean wind and wave climate. Int J Climatol 1999;19(9):931–50. http://dx.doi.org/10.1002/(SICI)1097-0088(199907)19:9<931::AID-JOC412>3.0.CO;2-O.